arXiv:astro-ph/9906394v1 24 Jun 1999

Statistical Analysis of Spectral Line Candidates in Gamma-Ray Burst GRB870303

P. E. Freeman[1,6], C. Graziani[1], D. Q. Lamb[1],
T. J. Loredo[2], E. E. Fenimore[3], T. Murakami[4],
A. Yoshida[5]

ABSTRACT

The *Ginga* data for the gamma-ray burst GRB870303 exhibit low-energy dips in two temporally distinct spectra, denoted S1 and S2. S1, spanning 4 seconds, exhibits a single line candidate at $\approx$ 20 keV, while S2, spanning 9 seconds, exhibits apparently harmonically spaced line candidates at $\approx$ 20 and 40 keV. The centers of the time intervals corresponding to S1 and S2 are separated by 22.5 seconds. We rigorously evaluate the statistical evidence for these lines, using phenomenological continuum and line models which in their details are independent of the distance scale to gamma-ray bursts. We employ the methodologies based on both frequentist and Bayesian statistical inference that we develop in Freeman et al. (1999b). These methodologies utilize the information present in the data to select the simplest model that adequately describes the data from among a wide range of continuum and continuum-plus-line(s) models. This ensures that the chosen model does not include free parameters that the data deem unnecessary and that would act to reduce the frequentist significance and Bayesian odds of the continuum-plus-line(s) model. We calculate the significance of the continuum-plus-line(s) models using the χ^2 Maximum Likelihood Ratio test. We describe a parametrization of the exponentiated Gaussian absorption line shape that makes the probability surface in parameter space better-behaved, allowing us to estimate analytically the Bayesian odds. We find that the significance of the continuum-plus-line model requested by the S1 data is 3.6×10^{-5}, with the odds favoring it being 114:1. The significance of the continuum-plus-lines model requested by the S2 data is 1.7×10^{-4}, with the odds favoring it being 7:1. We also apply our methodology to the combined (S1+S2) data. The significance of the continuum-plus-lines model requested by the combined data is 4.2×10^{-8}, with the odds favoring it being 40,300:1.

[1]Dept. of Astronomy and Astrophysics, University of Chicago, Chicago, IL 60637

[2]Dept. of Astronomy, Space Sciences Building, Cornell University , Ithaca, NY 14853

[3]Mail Stop D436, Los Alamos National Laboratory, Los Alamos, NM 87545

[4]Institute of Space and Astronautical Science, 1-1, Yoshinodai 3-chome, Sagamihara, Kanagawa 229, Japan

[5]Institute of Physical and Chemical Research, 2-1, Hirosawa, Wako, Saitama 351-01, Japan

[6]Presented as a thesis to the Department of Astronomy and Astrophysics, The University of Chicago, in partial fulfillment of the requirements for the Ph.D. degree.

Subject headings: line: identification — gamma rays: bursts

1. Introduction

The cause of gamma-ray bursts (GRBs) remains a mystery, a quarter century after the announcement of their discovery by Klebesadel, Strong, & Olson (1973). The recent discovery of optical transients associated with GRBs (e.g. van Paradijs et al. 1997 and references therein), and the apparent determination of redshifts for five of them−GRB970508 (Metzger et al. 1997), GRB971214 (Kulkarni et al. 1998), GRB980613 (Djorgovski et al. 1999), GRB980703 (Djorgovski et al. 1998), and GRB 990123 (Kelson et al. 1999)−have indicated that some (if not all) GRBs occur at cosmological distances. (While Ockham's Razor might lead one to conclude on the basis of the available evidence that all bursts are cosmological, it is important to remember that the GRB sky location data themselves do not yet rule out a separate galactic GRB source population; see, e.g., Loredo & Wasserman 1995, 1998a,b.) While broad-band observations indicate that relativistically expanding fireballs can explain the spectral and temporal behavior of these cosmological transients (Goodman 1986; Mészáros & Rees 1997), it is the study of low-energy ($\lesssim$ 100 keV) spectral line candidates seen in the spectra of other GRBs that can potentially provide the most powerful means both to determine how cosmological and/or galactic GRBs occur and to place constraints on their environments.

Mazets et al. (1980, 1981) were the first to report low-energy spectral line candidates. They found single dips and troughs in the spectra of 19 bursts detected by the Konus detectors on *Venera 11* and *Venera 12*.[7] This corresponds to $\approx 15\%$ of the bursts detected by Konus. The statistical significances of these features have not been reported. Hueter (1987) then reported single low-energy dips with modest statistical significance ($\sim 10^{-3}$) in spectra of two bursts out of 21 detected by the *HEAO-1* A4 detector. These reports influenced the design of the Los Alamos/ISAS Gamma-Ray Burst Detector (GBD; Murakami et al. 1989) on the *Ginga* satellite. To help analysts differentiate spectral lines from changes in continuum shape, a proportional counter (PC) covering the energy range $\approx 1.5 - 30$ keV was included as part of the GBD, in addition to a scintillator counter (SC) covering $\approx 15 - 400$ keV. (For Konus and *HEAO-1* A4, $E_{\rm low} \gtrsim 20$ keV.) The spectra of three bursts observed by the GBD−GRB870303 (spectrum S2), GRB880205 (spectrum b), and GRB890929−were found to exhibit apparently harmonically spaced absorption-like line candidates at ≈ 20 and 40 keV (Murakami et al. 1988, hereafter M88; Fenimore et al. 1988; Yoshida et al. 1991). This is out of 23 bursts examined overall. Another spectrum from an earlier epoch of GRB870303, denoted S1, was found to exhibit a single absorption-like line candidate at ≈ 20 keV (Graziani et al. 1992, 1993, hereafter G92 and G93 respectively). Analyses of the GRB880205 and GRB890929 spectra established the significance of the line candidates to be $\approx 9 \times 10^{-6}$ and $\approx 3 \times 10^{-3}$, respectively (Fenimore et al.; Wang et al. 1989; Yoshida et al.). An analysis of

[7]An additional burst with an apparent trough was later determined to be a solar flare; see Atteia et al. 1987.

GRB870303 established the significance of the line candidates in the spectra S1 and S2 to be $\approx 1.1 \times 10^{-6}$ and $\approx 2.1 \times 10^{-4}$, respectively (G92; we correct the values they report, as they used an incorrect number of degrees of freedom when calculating significances).

Since *Ginga*, no GRB detectors possessing the low-energy sensitivity of the GBD have flown. Of those that have flown, the ones which are in principle the most capable of detecting line candidates are the eight Spectroscopy Detectors (SDs) of the Burst and Transient Source Experiment (BATSE), on the *Compton Gamma-Ray Observatory*. The gain settings of the individual SDs differ; those with the highest gain settings can, in principle, observe GRBs at energies $\gtrsim 10$ keV. An electronic artifact discovered after launch affects energy calibration such that spectra are distorted in the first ≈ 10 channels above the low-energy cutoff (the so-called "SLED" effect; see Band et al. 1992). While this can possibly affect line detection, studies using simulated *Ginga* line candidate spectra indicated that the BATSE SDs were still capable of detecting low-energy spectral line candidates (Band et al. 1995). However, no line candidates were definitively detected during initial visual searches of those BATSE SD spectra with the largest signal-to-noise ratios (Palmer et al. 1994, Band et al. 1996). The criteria for detection included having the candidate appear in the data from at least one SD with F-test significance $\leq 10^{-4}$, with the contemporaneous data collected in other SDs being consistent with the continuum-plus-line(s) model. An automated line candidate search algorithm designed by the BATSE SD team (Briggs et al. 1996) was then applied to spectra in 117 bright bursts for which there is at least one spectrum with signal-to-noise > 5 at ≈ 40 keV (Briggs et al. 1998). This automated search, which is considerably more sensitive than a visual search, yielded 12 candidate spectral line candidates for which the change in χ^2 between the continuum and continuum-plus-line fits is > 20 (significance $< 5 \times 10^{-5}$). All candidates are emission-like lines at ≈ 40 keV, with one absorption-like line candidate at ≈ 60 keV. While Briggs et al. estimate the ensemble chance probability of the most-significant feature as $\lesssim 10^{-3}$, and state that few of these features, if any, result from statistical fluctuations, these should not be considered definitive detections, as the contemporaneous data from other SDs is still being examined (Briggs et al. 1999).

In sum, the *Ginga* observations provide strong evidence for spectral lines that has as yet neither been independently confirmed, nor refuted. There is, however, a theoretical bias against the existence of lines, reinforced by the strong evidence supporting a cosmological distance scale for GRBs. This has developed because few cosmological burst models have attempted to account for the existence of harmonically spaced lines (see, e.g., Stanek, Paczyński & Goodman 1993, and Ulmer & Goodman 1995, who attempt to account for lines by invoking gravitational femtolensing). However, the simple lack of theoretical models does not, nor cannot, rule out the possibility of spectral lines in cosmological burst spectra. In the galactic GRB paradigm, harmonically spaced absorption-like lines are relatively simple to explain, using cyclotron resonant scattering in the strong magnetic field ($B \sim 10^{12}$ G) of a neutron star. Quantization of an electron's energy perpendicular to the magnetic field B facilitates the formation of harmonically spaced lines with a spacing $\Delta E \approx 11.6 B_{12}$ keV. (See, e.g, Fenimore et al.; Wang et al.; Alexander and Mészáros 1989; Miller et al. 1991, 1992; Isenberg, Lamb, & Wang 1998; and Freeman et al. 1999a, hereafter Paper II.)

In this paper, we present rigorous methods of statistical inference that the reader may use to firmly establish the evidence for spectral lines in GRB spectra, using simple phenomenological models that are *independent of the underlying physics of, and distance scale to, GRBs*. To illustrate these methods, we apply them to the spectral line candidates exhibited by the S1 and S2 spectra of GRB870303. In a companion paper (Paper II) we physically interpret these line candidates within the galactic GRB paradigm, using the cyclotron resonant scattering line transfer code originally developed by Wang, Wasserman, & Salpeter (1988).

In §2 we describe the *Ginga* GBD and its observation of GRB870303. In §3, we present a basic introduction to the statistical concepts that we use in this paper. These concepts are discussed in greater detail in Freeman et al. (1999b), hereafter Paper III. In that work, we present general, rigorous, methodologies that address the problem of establishing the existence of a line in a spectrum, that are based upon both the so-called "frequentist," and Bayesian, paradigms of statistical inference. We apply both frequentist and Bayesian methodologies in this work to ensure robust conclusions. In §4 we describe the method by which we select the simplest continuum model that fits to the data outside the line candidate(s) (rather than, e.g., simply assuming a continuum spectral shape). We consider a wide range of spectral models, which assures that our conclusions are robust. Continuum model selection for *Ginga* GBD data is complicated by the presence of spectral rollover at energies $\lesssim 5$ keV, which we do not wish to model, and we show how we adapt our method to determine which PC bins may be included in fits. In §5, we describe how we select the simplest continuum-plus-line(s) model that adequately fits to the data. We introduce a parametrization of the exponentiated Gaussian line in terms of its equivalent width $W_{\rm E}$ and full width at half maximum $W_{\frac{1}{2}}$, the use of which results in a more well-behaved likelihood surface. The model and its parametrization allows us to treat saturated lines and, in addition, to apply analytic Bayesian inference to both saturated and unsaturated lines. We demonstrate the importance of applying models with as few free parameters as possible, by applying saturated lines (with two, rather than three, free parameters), and/or by harmonically linking parameters between two lines, in fits to these moderate resolution data. We compare the selected continuum-plus-line(s) model to the selected continuum model to evaluate the frequentist statistical significance, and the Bayesian odds in favor, of the best-fit continuum-plus-line(s) models for GRB870303 S1 and S2. We also determine the frequentist confidence and Bayesian credible regions for the parameters of these best-fit continuum-plus-line(s) models. In §6 we discuss our results.

2. Observation of GRB870303

We first summarize the characteristics of the *Ginga* GBD; the interested reader will find more details in Murakami et al. (1989). The passively shielded and non-collimated GBD contained two co-aligned instruments for detecting GRB photons. The Proportional Counter (PC), used to detect low-energy photons, consisted of a 3-cm deep Xe-CO_2 gas reservoir, with geometric area ≈ 63 cm^2. The Scintillation Counter (SC), used to detect higher-energy photons, consisted of a 1-cm thick

NaI crystal with geometric area ≈ 60 cm^2, backed by a 7.6-cm diameter phototube. The entrance window of the SC was covered by a 0.2-mm-thick aluminum sheet, whereas the entrance window of the PC was covered with a 63.5-micron-thick layer of beryllium, which has greater transparency than an aluminum layer of similar thickness at low energies. In both instruments, an incident photon triggers an electron pulse; the intensity of the pulse (the pulse height) is then used to discern the amount of energy deposited by the photon. Because the photon may not deposit all its energy in these detectors, the PC and SC record the number of counts as a function of photon *energy loss*, in 16 and 32 semi-logarithmically spaced bins, respectively. To avoid the effect of uncertain discriminator settings, we do not consider the lowest and highest energy-loss bins in each detector (Murakami, private communication). Excluding these bins, the PC and SC cover 1.4-23.0 keV and 16.1-335 keV, respectively, for the gain setting at the time that GRB870303 occurred. At the line candidate energy of ≈ 20 keV, the energy resolution of the PC and SC are ≈ 3.4 and 5 keV, respectively; at 40 keV, the resolution of the SC is ≈ 8.4 keV.

The GBD detected GRB870303 at 16:23 UT on 3 March 1987. Figure 1 shows burst-mode time history data for the PC and SC. The GBD continuously recorded burst-mode data at 0.5-second intervals. These data were not stored in memory until a burst was detected, at which time the data from 16 seconds prior to the burst trigger until 48 seconds after the burst trigger were stored. The peak count rate (determined within a 4 second interval) in the SC is ≈ 379 cts s^{-1}. The background rate in the SC is ≈ 572 cts s^{-1}. In addition to burst-mode data, the GBD also continuously recorded the gamma-ray background in real-time mode, which had a coarse time resolution (usually 16 seconds). These data are used to estimate the background count rate during the burst, in each energy-loss bin. By analyzing 150 seconds of real-time data from before the burst, and 220 seconds of real-time data from after the burst, we determine that the background amplitude is constant as a function of time throughout the burst interval.

The background-subtracted spectral data for GRB870303 exhibit line candidates during two time intervals, the spectra of which we denote S1 and S2 (following G92). Figure 2 shows both spectra. S1 is constructed from 4 seconds of data, during which the burst had energy fluence 1.3×10^{-6} erg cm^{-2} in the bandpass 50-300 keV. (This fluence is estimated from the best-fit model; Table 6.) It exhibits a saturated line candidate at ≈ 20 keV. S2 is constructed from 9 seconds of data, during which the burst had energy fluence 4.5×10^{-6} erg cm^{-2}. It exhibits two harmonically spaced line candidates, at ≈ 20 and 40 keV. The midpoints of the time intervals from which S1 and S2 are constructed lie 22.5 seconds apart.

Neither the PC nor SC could intrinsically determine the angle of incidence of burst photons relative to the detector normal, $\theta_{\rm inc}$. The burst detector on the *Pioneer Venus Orbiter (PVO)* also observed GRB870303; combining the photon time-of-arrival information from the *Ginga* and *PVO* spacecraft limits the possible directions of the burst to an annulus on the sky. The burst photon angle of incidence is thus constrained to lie within the range $11.2^\circ \lesssim \theta_{\rm inc} \lesssim 57.6^\circ$ (Yoshida, private communication, correcting Yoshida et al. 1989). In their analyses of the GRB870303 data, M88, G92, and G93 assume $\theta_{\rm inc} = 37.7^\circ$. Since the shape and amplitude of a model counts spectrum

that is derived from a given photon spectrum depends sensitively on $\theta_{\rm inc}$, we treat this angle as a freely varying model parameter in this work. Because *Ginga* response matrices are computed using computationally intensive Monte Carlo simulations, we use a grid of fixed values $0.54 \leq \cos\theta_{\rm inc} \leq 0.98$, with $\Delta(\cos\theta_{\rm inc}) = 0.02$. This grid is sufficiently dense to allow us to accurately determine statistical quantities such as line significance (see, e.g., Figure 6).

3. Statistical Principles

We analyze the line candidates in the spectra of GRB870303 S1 and S2 using both frequentist and Bayesian methods of model comparison and parameter estimation. In this section, we provide a basic introduction to those elements of frequentist and Bayesian statistical inference relevant for the analysis of gamma-ray burst spectral lines. The reader will find more detail on these methods in Paper III and references therein.

3.1. Model Comparison

3.1.1. Frequentist Method

The frequentist comparison of two models, the null hypothesis H_0 and the alternative hypothesis H_1, is carried out by constructing a test statistic T, which is usually a function of the goodness-of-fit statistics for both models. There are two probability distribution functions, or PDFs, which indicate the a priori probability that we would observe the value T, computed assuming the truth of H_0 and H_1, respectively. The test significance, α, or Type I error, is calculated by computing the tail integral of the H_0 PDF from T to infinity. The resulting number represents the probability of selecting the alternative hypothesis H_1 when in fact the null hypothesis H_0 is correct; if the number is sufficiently small, we reject H_0 in favor of H_1. A common threshold for rejecting the null hypothesis is $\alpha \leq 0.05$, though in this work we use more conservative threshold values.

For the particular case of GRB spectral analysis, the appropriate sampling distribution for the data is the Poisson distribution, and the likelihood function $\mathcal{L}$, the product of Poisson probabilities for the data in each bin, given model count rates, provides the best means to assess the viability of a model. H_0 is the model with no line(s), H_1 is the model with line(s), and $T = \frac{\mathcal{L}_{\rm max}(H_1)}{\mathcal{L}_{\rm max}(H_0)}$. (The best-fit point, or mode, in parameter space is where the likelihood function is maximized.) To determine the H_0 PDF, one would simulate large numbers datasets from the best-fit model for H_0 (i.e. with the model parameters set to best-fit values), and determine the distribution of observed values of $T_{\rm sim}$. After the H_0 PDF is determined, finding the significance α is trivial.

However, this process may be computationally intensive. So the frequentist often falls back upon the understanding that in the limit of a large number of counts n in a bin, the Poisson

distribution is very nearly Gaussian with a standard deviation "root-n". This understanding, in principle, allows the use of Pearson's χ^2 statistic, an approximation of $L = \log \mathcal{L}$, to assess models:

$$s^2 \;=\; \sum_{i=1}^{N} \frac{(m_i - n_i)^2}{\sigma_i^2}. \tag{1}$$

The sum extends over N data bins, and m_i and n_i are the predicted and observed counts in bin i, respectively. The best-fit parameters for a given model are those for which s^2 is minimized. This statistic has the advantage that analytic formulae may be available to determine line candidate significance. Under the same assumption of a paraboloidal log-likelihood function in parameter space, s^2 is sampled from the χ^2 PDF (in this paper, we follow the notation of Lampton, Margon, & Bowyer 1976, who reserve the symbol χ^2 for a statistic which is explicitly sampled from the χ^2 distribution). There is some ambiguity in the choice of σ_i: two widely used choices are $\sigma_i^2 = n_i$ ("data variance"), and m_i ("model variance"). We denote fit statistics using these two variance choices as $s^2_{\rm d}$ and $s^2_{\rm m}$, respectively.

In this work, we compare models H_0 and H_1 using the χ^2 Maximum Likelihood Ratio (χ^2 MLR) test (Eadie et al. 1971, pp. 230-232). In Paper III, we demonstrate that the use of this test results in fewer Type I errors than both the F-test and the χ^2 Goodness-of-Fit (GoF) test. It is also the most powerful test (Eadie et al., pp. 219-220). In order to use it, the simpler model must be nested within the more complicated alternative model, i.e. the simpler model must be obtainable by setting the extra $\Delta P \equiv P_1 - P_0$ parameters of the alternative model to default values, often zero. The χ^2 MLR test statistic is $\Delta s^2 \equiv s^2(H_0) - s^2(H_1)$. If the Gaussian approximation is valid, $p(\Delta s^2|H_0)$ is given by the χ^2 distribution for ΔP degrees of freedom.

A sufficient condition that s^2 is distributed as χ^2 ($s^2 \sim \chi^2$) is that $p(n_i|m_i)$ be Gaussian with mean m_i and width σ_i. This condition is not met if we fit a continuum-only model to data that has a pronounced absorption-like or emission-like line candidate, regardless of the choice of variance: we will be calculating the significance with which H_0 is to be rejected in the regime where the χ^2 approximation to the likelihood breaks down. (This is because a second-order Taylor series expansion of the Poisson log-likelihood, as a function of, e.g., $\delta \equiv \frac{|n_i - m_i|}{\sqrt{m_i}}$, is not sufficiently accurate when $\delta \gtrsim \sqrt{m_i}$; additional terms must be included. It is precisely the second-order expansion which can be recast as χ^2.) Consequently, the significance calculated by looking up Δs^2 in the χ^2 distribution with ΔP degrees of freedom cannot be expected to agree with the "true" significance, i.e., the tail integral of the true H_0 PDF determined using the Poisson likelihood function. For the case relevant for this paper, absorption-like line candidates, the use of model variances will cause the "true" significance to be underestimated,[8] while the use of variances derived from the data will lead to overestimates of the "true" significance (i.e., $\alpha_{\chi^2{\rm MLR},s^2_{\rm m}} > \alpha_{\mathcal{L}}$, and $\alpha_{\chi^2{\rm MLR},s^2_{\rm d}} < \alpha_{\mathcal{L}}$). As shown in Paper III, we have found that model variances provide a better estimate of the true significance, so we calculate variances from the model in this work.

[8]To avoid semantical confusion: the smaller the value of α, the greater the "significance," in a qualitative sense. Throughout this paper, we follow the convention that H_1 becomes "more significant" as $\alpha \to 0$.

Another problem with the use of the χ^2 MLR test is the condition that estimates for the values of the additional parameters introduced by H_1 must be drawn from normal distributions (Eadie et al., p. 232), as the line-centroid energy is drawn from uniform distribution over the detector bandpass (e.g. a spurious line could just as easily be seen at 100 keV as 20 keV). As discussed in Paper III, this tends to lessen the significance of any detected line (i.e. $\alpha_{\mathcal{L},\mathrm{true}} > \alpha_{\mathcal{L}}$). The magnitude of the decrease in significance is dependent on the number of data bins and the width of the line. Our simulations indicate that for the specific case of the *Ginga* GBD, $\alpha_{\chi^2\mathrm{MLR},s_m^2} \approx \alpha_{\mathcal{L},\mathrm{true}}$.

3.1.2. Bayesian Method

As noted above, the appropriate sampling distribution for counts data is the Poisson distribution, and the likelihood function $\mathcal{L}$, the product of Poisson probabilities for the data in each bin, given model count rates, provides the best means to assess the viability of a given model M. The viability of a model in the frequentist method is assessed in part by maximizing the likelihood function, but in the Bayesian method, we integrate the likelihood function over the P-dimensional model parameter space. The resulting quantity is called the average likelihood:

$$p(D|M,I) \;=\; \int dx\; p(x|M,I)\; p(D|M,x,I) \;=\; \int dx\; p(x|M,I)\; \mathcal{L}(x). \tag{2}$$

In this equation, D represents the data, while x represents the freely varying parameters of model M, and I represents information relevant to the analysis (e.g. detector bandpass). The likelihood is weighted at each point in parameter space by the conditional probability $p(x|M,I)$, called the prior probability, or simply the prior. The prior is a quantitative statement of our state of knowledge about the relative probability of each possible value of the parameter x before the data are examined. There is a large body of literature on the subject of how to assign priors (see Loredo 1992 and references therein), which we will not summarize here. When possible, we prefer to use "least informative" uniform priors (i.e. constant amplitude functions), with finite bounds which are determined in a physically meaningful way (see Appendix B).

Bayes' Theorem allows us to calculate the posterior probability $p(M|D,I)$ for model M, given its average likelihood:

$$p(M|D,I) \;=\; p(M|I)\frac{p(D|M,I)}{p(D|I)} \tag{3}$$

Here, $p(M|I)$ is the prior of the model itself (as opposed to the values of each of its parameters), and $p(D|I)$ is a normalization factor. A large posterior probability indicates support for the given model. Instead of computing such a probability directly, we determine the ratio of posterior probabilities for any two models within a specified set of models $\{M_i\}$. This quantity is called the *odds*:

$$O_{21} \;=\; \frac{p(M_2|D,I)}{p(M_1|D,I)} \;=\; \frac{p(M_2|I)}{p(M_1|I)}\frac{p(D|M_2,I)}{p(D|M_1,I)} \;=\; \frac{p(M_2|I)}{p(M_1|I)}B_{21}. \tag{4}$$

Benefits of computing the odds are that we can ignore the normalization $p(D|I)$, and, if we do not have a priori preferences for either model, the model priors $p(M_i|I)$. The ratio of average

likelihoods, denoted B_{21} above, is termed the Bayes factor. A Bayes factor of >10-20 is considered strong evidence in favor of the alternative model, while a Bayes factor in excess of 100 is considered decisive (see the review by Kass & Raftery 1995 and references therein).

Generally, the odds must be computed using numerical methods. However, if the shape of the likelihood surface in parameter space is similar to that of a multi-dimensional Gaussian function, we may use the Laplace approximation to estimate the average likelihood (see, e.g., Kass & Raftery, Loredo & Lamb 1992):

$$p(D|M_i, I) \;=\; p(\hat{x}_{i,1} \cdots \hat{x}_{i,P_i}|I)(2\pi)^{P_i/2}\sqrt{\det V_i}\mathcal{L}_i^{\max} \tag{5}$$

V_i is the covariance matrix, determined by inverting the matrix of likelihood function second derivatives evaluated at the mode. To derive eq. (5), we first assume that the prior does not vary markedly around the mode, so that the prior term in the integrand of eq. (2) may be replaced a constant evaluated at the mode. (The hats placed on the parameters x signify that we adopt their values at the mode when evaluating the prior.) What is left in the integrand is the integral of $\mathcal{L}_i$, which we assume has multi-dimensional Gaussian shape: $\mathcal{L}_{i,\max} \times G(x_i)$. Since $G(x_i)$ is an unnormalized Gaussian function, its integral is $(2\pi)^{P_i/2}\sqrt{\det V_i}$.

We thus approximate the odds as

$$O_{21} \;=\; e^{\Delta L}(2\pi)^{\Delta P/2}\sqrt{\frac{\det V_2}{\det V_1}}\frac{p(\hat{x}_{2,1} \cdots \hat{x}_{2,P_2}|I)}{p(\hat{x}_{1,1} \cdots \hat{x}_{1,P_1}|I)}. \tag{6}$$

(In this expression we use the log-likelihood, $L = \log \mathcal{L}$.) This expression is sufficiently accurate-generally correct to within a factor of two even if the likelihood surface deviates somewhat from the ideal Gaussian shape-to allow us to draw firm conclusions about the relative ability of the two models to represent the observed data.

3.2. Parameter Estimation

3.2.1. Frequentist Method

We employ the method of projection to determine frequentist confidence intervals (Eadie et al.; Lampton et al.). For a given parameter, we construct a set of values, and at each point on the set, we minimize $s_{\rm m}^2$ with respect to the remaining parameters. If the shape of the likelihood surface in parameter space is similar to that of a multi-dimensional Gaussian function ($\mathcal{L} \propto \exp[-\Delta s_{\rm m}^2/2]$), and if the value of the likelihood at the mode is much larger than the maximum value of the likelihood along the parameter space boundary, then the $n\sigma$ confidence interval for an individual parameter is given by those values of the fixed parameter such that $s_{\rm m,proj}^2 = s_{\rm m,min}^2 + n^2$.

If the likelihood surface deviates markedly from the ideal Gaussian shape, such that it cannot be cast into that shape by parameter transformation, or if the likelihood surface intersects parameter

space boundary near the mode, the formula $\Delta s^2_{\rm m} = n^2$ will not apply. (In the particular case of an otherwise well-behaved likelihood surface which is cut off at a parameter space boundary, the value Δs^2 which defines the $n\sigma$ confidence interval is $< n^2$; the use of $\Delta s^2_{\rm m} = n^2$ will thus lead to overestimates of the confidence interval size.) In these situations, we must perform simulations to accurately determine the confidence intervals. This is because the random variables in frequentist theory are the data, and not the model parameters: we may not integrate over parameter space in an attempt to make inferences about the parameters.

3.2.2. Bayesian Method

We may determine a Bayesian credible interval for a particular parameter x of model M, without reference to the other, "uninteresting," parameters, collectively denoted x', by *marginalizing* the posterior function $p(x, x'|D, I)$ over the space of parameters x':

$$p(x|D, I) \propto \int dx' p(x, x'|I) p(D|x, x', I). \tag{7}$$

We use the proportionality symbol because we ignore the normalization factor $p(D|I)$. The credible interval is defined as

$$z \;=\; \frac{\int_{x_1}^{x_2} dx p(x|D, I)}{\int_{{\rm all}x} dx p(x|D, I)}, \tag{8}$$

where z is the desired probability content (e.g. 0.683 for 1σ bounds), and $p(x_1|D, I) = p(x_2|D, I)$.[9] Note that in the frequentist theory of confidence intervals, $p(x_1|D, I)$ does not have to equal $p(x_2|D, I)$ (though they are equal in the projection method described above), which means that confidence intervals, unlike credible intervals, are not unique. Only when the log-likelihood function is paraboloidal in parameter space will the Bayesian method yield the same result as the frequentist projection method.

Even if the shape of the likelihood surface is nearly Gaussian, numerical integration of the posterior to determine credible intervals is preferable to the use of the Laplace approximation (eq. 6), since the latter may not give sufficiently precise answers. Numerical integration may not be feasible, however, if the number of model parameters becomes too large ($\gtrsim 5$). To use the Laplace approximation in this case, we would select a grid of fixed values for the parameter x, and at each grid point compute

$$p(x|D, I) \;=\; p(x, \hat{x}'|I)(2\pi)^{P_i - 1/2} \sqrt{{\rm det}V(x, \hat{x}')} {\rm exp}[L(x, \hat{x}')]. \tag{9}$$

After we compute $p(x|D, I)$ at each point on the grid, we would use eq. (8) as before to determine credible interval bounds.

---

[9]Here we implicitly assume the likelihood surface is smooth and unimodal, so that any particular value $p(x|D, I)$ occurs no more than twice.

4. Continuum Analysis

In order to compare models with and without lines, and to estimate the parameters of the lines (if lines are detected), we must specify a continuum model. The radiative processes that produce the continuum spectrum of gamma-ray bursts are unknown. Therefore, any physically reasonable form for the continuum spectrum is a possibility. And we regard all models of burst continuum spectra, even when of a form (such as power law or power law times exponential) produced by known radiative processes, as purely phenomenological. We consider a wide range of possible continuum models, in order that we may draw relatively robust conclusions from our study.

An unnecessarily complicated continuum model can reduce the frequentist significance of a line, and the Bayesian odds favoring a model with a line over one without. *It is therefore important to select the simplest continuum model that adequately describes the data.* In this section, we discuss the procedure that we use to select continuum models.

4.1. Exclusion of the Energy-Loss Bins Affected by the Candidate Line

In selecting the simplest continuum model that adequately describes the data, we exclude those energy-loss bins associated with the line candidate(s) from the fits, in order not to bias the outcome. To determine which energy-loss bins to exclude from fits, we first examine the raw data by eye to determine the approximate line-centroid energy, E_c, of a candidate line. An incident photon at this energy has probability p_i of being recorded as a count in the $i^{\rm th}$ energy-loss bin. If $p_i > 0.1$, we exclude the $i^{\rm th}$ bin from fits. Using this criterion, we exclude from the continuum model fits bins PC 14-15 and SC 2-6 from the spectrum S1 and bins PC 14-15, SC 2-6, and SC 10-14 from the spectrum S2.

4.2. Continuum Model Selection

In this section, we illustrate how we apply frequentist statistical methodology to the selection of best-fit continuum models for the S1, S2, and combined (S1+S2) data. Later, in our Bayesian analyses of the line candidates exhibited by these data, we adopt the continuum model selected using this frequentist method. We do this because the calculation of Bayesian odds favoring one continuum model over another requires the stipulation of limits on the allowed range of each continuum parameter, so that we may compute its prior. Because the GRB continuum models are entirely phenomenological, it is difficult to place meaningful, physically-motivated, limits on the priors (e.g., how should we determine the limits on a power law slope?). We stress that the decision not to apply Bayesian methodology to continuum model selection reflects our bias against using subjectively chosen priors for model parameters, and should not be viewed by the reader as an absolute injunction against the use of the Bayesian methodology to select continuum models when

analyzing gamma-ray burst data.

We show our continuum model selection algorithm in Figure 3. The selection of the best-fit continuum model is straightforward (Figure 3a). We fit each of a specified set of continuum models M_i to the data. (Because we exclude from these fits the energy-loss bins in the vicinity of the line candidate(s), where the model may not represent the data well, and thus where the approximations used to derive $s^2_{\rm m}$ from $\mathcal{L}$ may be violated, we can use the fitting statistic $s^2_{\rm m}$ [see §3].) If two or more models have the same number of free parameters, we choose the one which fits to the data with the lowest value $s^2_{\rm m}$. Beginning with the simplest model (i.e. the one with the fewest number of free parameters), we compute the significance of $\Delta s^2_{\rm m}$ for each alternative model by computing $\alpha_{\chi^2{\rm MLR}}(\Delta s^2_{\rm m}, \Delta P)$, where ΔP is the number of additional free parameters introduced by the alternative model. If $\alpha_{\chi^2{\rm MLR}}$ is never ≤ 0.01, we select the simplest model; otherwise, we choose the simplest alternative model, and compare that model against all remaining more complex alternative models. We repeat this process until a continuum model is selected.

Complicating the process of continuum selection is the fact that the magnitude of photon absorption in the beryllium window of the GBD PC, at low energies ($E \lesssim 5$ keV), depends sensitively upon the burst photon incidence angle $\theta_{\rm inc}$. As previously stated, for GRB870303 this angle lies within the interval $11.2^\circ \lesssim \theta_{\rm inc} \lesssim 57.6^\circ$. Thus, for $E \lesssim 5$ keV, we cannot disentangle the absorption caused by the window from any rollover intrinsic to the burst spectrum and any absorption that may occur in intervening cold interstellar gas. Modeling the spectral rollover thus greatly complicates the fitting process while leaving our conclusions about the line candidates essentially unaffected. Hence, we add a step to the continuum selection algorithm which allows us to determine which energy-loss bins are most effected by the rollover (Figure 3b), and we exclude these bins from subsequent line candidate analysis. We model the spectral rollover using phenomenological absorption by a cold interstellar gas with a column density N_H (model NH in Table 1). We start by fitting to the data in all available PC bins (PC 2-13). If the selected best-fit model includes the rollover parameter, we eliminate the lowest-energy bin and repeat the process of model selection, continuing until the data select a continuum model without rollover.

In our fits, we consider four phenomenological continuum models (Table 1). The four-parameter "Band et al. model" (Band et al. 1993) adequately describes all BATSE SD spectra to which it has been applied. The bandpasses of the BATSE SDs extend to much higher energies than did the bandpass of the GBD SC, so the SC data for GRB870303 may be insufficiently informative to require that the the exponential cutoff energy, and/or second power law slope, of this model be specified. Thus, we consider two simpler models nested within the Band et al. model: a three-parameter power-law times exponential (PLE) model; and a two-parameter power law (PL) model. We also consider a two-segment broken power law (BPL) because G92 and G93 use it to model the continuum of S2. (This complicates the model comparison process because the PLE model is not nested within the BPL model, so that they are not directly comparable using the χ^2 MLR test. But we never find the BPL and BPL+NH models to be the best-fit models amongst models with 4 and 5 free parameters, respectively.) In our fits, we vary the logarithms of the normalization and

energy parameters, so that the shape of likelihood surface is more nearly Gaussian. We also apply a "pivot" energy of 20 keV (e.g., for the PL model, we use the formula $\frac{dN}{dE} = AE^{-\alpha} = A'(E/20)^{-\alpha}$). This helps reduce the size of the confidence and credible intervals for the highly correlated parameters A and α, while also improving likelihood surface behavior. Applying this set of models within our continuum selection algorithm, we determine that the PL and PLE models are the best-fit continuum models for S1 and S2 respectively (Table 2).

We use a similar algorithm to select continuum model(s) and bin ranges for the fit to the combined (S1+S2) data. This process of model selection is considerably more complicated because we must both determine whether the data explicitly request different values for some continuum parameters common to both fits (e.g. power law slope, if we fit the PL model to S1 and the PLE model to S2), and we also must determine whether the data explicitly request separate burst photon incidence angles $\theta_{\rm inc}$ for the two datasets. We determine that the data select the PL model for S1 and the PLE model for S2, with separate normalizations and power law slopes (Table 2).

We note that the PL model fits to the data of GRB870303 S1 with $s^2_{\rm m} = 18.22$ for 28 degrees of freedom. This value of $s^2_{\rm m}$ is strikingly small: if $s^2_{\rm m} \sim \chi^2$, then the probability of finding this or a lower value of $s^2_{\rm m}$ is 0.080. (G92, who use $s^2_{\rm d}$, a different choice of energy-loss bins, and assume $\theta_{\rm inc}$ = 37.7°, compute a probability 0.023.) While this is not technically a significantly low value of $s^2_{\rm m}$, we point out that extensive studies of the GBD were done which demonstrate that instrumental effects such as dead time, pulse pileup, or bin overlap in the GBD did not conspire to lower the value of s^2 (e.g. Graziani 1990). Furthermore, a detailed analysis of GRB870725, a burst which occurred while *Ginga* was passing over the Kagoshima Ground Station, showed that the burst mode and real time data were still in complete agreement nearly five months after GRB870303.

5. Line Analysis

5.1. Line Model

When fitting a candidate line in the spectrum of a GRB, one must choose both a line model and a parametrization of that model. Astrophysicists often use either an additive Gaussian line, $AL(E) = C(E) - \beta G(E)$, or an exponentiated Gaussian line, $EL(E) = C(E)\exp(-\beta G(E))$, to model the line. (We use the symbols AL and EL to denote line fluxes so as to avoid confusion with the log-likelihood L.) C(E) is the continuum flux, and

$$G(E) \;=\; \exp\left(-\frac{(E-E_{\rm n})^2}{2\sigma^2}\right) \tag{10}$$

is the Gaussian line shape; $E_{\rm n}$ is the line-centroid energy of the nth harmonic line; and β and σ are the unnormalized strength and width of the Gaussian. We use the exponentiated line model rather than the additive Gaussian model because the flux in the latter can be negative, which is unphysical.

The exponentiated Gaussian model can be parametrized in different ways; the choice of the parametrization affects the shape of the likelihood surface in parameter space. Figure 4 shows contours of constant probability density as a function of (β,σ) from fitting to an incident photon spectrum with a given set of line parameters. The contours show that in this particular case (and in general) the likelihood surface will not have the shape of a multi-dimensional Gaussian function; if it did have this shape, we would observe elliptical contours. (Note that the axes of the ellipses are not required to be parallel to parameter axes.) In frequentist statistics, the parametrization of the line does not affect the calculated line significance (which depends only on $\Delta s^2_{\rm m}$), but it does affect the computation of confidence intervals. The projection method gives a confidence region that is accurate only if the shape of the likelihood surface closely approximates that of a multi-dimensional Gaussian. It is also advantageous because it greatly reduces the computational burden of calculating credible regions using Bayesian inference by allowing us to use the approximate expression in eq. (6) to determine the odds favoring the continuum-plus-line model.

While many parametrizations are well-behaved when the S/N of the spectrum is large and/or the line is strong (but not saturated), parametrizing the line in terms of its equivalent width, $W_{\rm E}$, and full-width at half-maximum, $W_{\frac{1}{2}}$, has many advantages compared to parametrizing it in terms of β and σ. First, we find that, when we take two-dimensional slices of the parameter space and plot the probability density contours corresponding to 2 and 3σ, parametrization of the line in terms of $W_{\rm E}$ and $W_{\frac{1}{2}}$ yields elliptical contours over a much larger range of count rates than does parametrization in terms of β and σ (see Figure 4). Second, it has the added advantage that it is more intuitive, in the sense that the visual shape of the line is related more directly to $W_{\rm E}$ and $W_{\frac{1}{2}}$ than to β and σ. Third, parametrization of the line in terms of $W_{\rm E}$ and $W_{\frac{1}{2}}$ is useful because the $W_{\frac{1}{2}}$ of the line candidates in the spectra of gamma-ray bursts is typically less than or of order the energy resolution of the detector, so that the detector is sensitive to $W_{\rm E}$ but not to $W_{\frac{1}{2}}$ (see below). We discuss the details of this parametrization in Appendix A.

5.2. Selection of the Line Model

G93 point out that the standard line parametrization becomes degenerate for saturated lines: for such lines, vast ranges of (very large values of) β and of (very small values of) σ result in lines which are virtually indistinguishable from each other using moderate resolution NaI crystal spectrometers. For example, if we convolve a Gaussian line of width σ with a Gaussian detector response of width σ_R, then for $\sigma \lesssim \sigma_{\rm R}$, the width of the final Gaussian line is $\approx \sigma_{\rm R}$. Thus a saturated line may be adequately described by two parameters, its line-centroid energy E and its equivalent width $W_{\rm E}$. How wide a line must be before the third line parameter, the FWHM $W_{\frac{1}{2}}$, is requested by the data depends upon how informative they are; it is more likely to be requested if the S/N of the spectrum is high. In the present context, this means that the S2 data are more likely to request a third parameter than the S1 data.

This is important because inclusion of unnecessary line parameters reduces $\Delta s^2_{\rm m}$ and ΔL per

line parameter. Since the number of additional parameters in the continuum-plus-line(s) model relative to the continuum model affects the frequentist significance, and both the number of extra parameters introduced by the continuum-plus-line(s) model and their prior ranges affects the Bayesian odds, it is important to use the minimum number of line parameters necessary to describe the data adequately.

The optimal search strategy for detecting a single narrow line is therefore to fit to the data a two-parameter saturated line parametrized by $(E, W_{\frac{1}{2}})$, with the ratio $W_{\rm E}/W_{\frac{1}{2}}$ set to its maximum value, 1.015 (see Appendix A and Figure 5). We then check whether or not the data is adequately described by a saturated line by comparing this fit with one in which the line is parametrized in terms of E, $W_{\rm E}$, and $W_{\frac{1}{2}}$ (and β is constrained to be $< \beta_o$). To optimally detect apparently harmonically spaced lines, we want to reduce the number of freely varying line parameters to the minimum requested by the data. For two lines, the first step is to assume harmonic spacing between the lines; this reduces the number of free parameters from six to five. The next step is to assume that each line is saturated; this reduces the number of free parameters from five to three. To reduce the number of free parameters to two, we link the width of the first and second harmonics. For the purely historical reason that line widths were once interpreted as Doppler widths of absorption profiles (e.g. Fenimore et al. 1988), we assume $W_{\rm E,2} = 2W_{\rm E,1}$. We could just as easily assume $W_{\rm E,2} = W_{\rm E,1}$. Since the width of the second harmonic in S2 is smaller than the energy resolution at 40 keV, the values of $s^2_{\rm m}$ and $\mathcal{L}$ are relatively insensitive to the assumed relation between $W_{\rm E,1}$ and $W_{\rm E,2}$.

In Table 3 we list the line models that we consider when fitting the spectra S1 and S2.

The procedure that we use to compare these continuum-plus-line models is analogous to that used to compare continuum models, but with the following differences: we assume the continuum model and the range of PC energy-loss bins that we selected using continuum model comparison; and we restore to the fits the energy-loss bins that we excluded earlier because they were near the energy of the line candidate. We note that not all the models we use to fit to S2 are nested within each other, which precludes using the χ^2 MLR test to compute significances in some cases; however, the selection of the line model was not effected by this. Use of this procedure leads to selection of the saturated line model (with parameters E and $W_{\rm E}$) for both S1 and S2.

Because $\cos\theta_{\rm inc}$ takes on discrete values in our analyses, we must apply a variation of eq. (6) in our Bayesian method of line model selection. For any given value of $\cos\theta_{\rm inc}$, we use the Laplace approximation to estimate the parameter space integral; we then sum these integrals over all values of $\cos\theta_{\rm inc}$:

$$O_{21} \;=\; \frac{\sum_{\cos\theta_{\rm inc}} p(\hat{x}_{2,1}\cdots\hat{x}_{2,P_2}, \cos\theta_{\rm inc}|I)(2\pi)^{P_2/2}\sqrt{{\rm det}V_2(\cos\theta_{\rm inc})}\exp(L_2^{\rm max}[\cos\theta_{\rm inc}])}{\sum_{\cos\theta_{\rm inc}} p(\hat{x}_{1,1}\cdots\hat{x}_{1,P_2}, \cos\theta_{\rm inc}|I)(2\pi)^{P_1/2}\sqrt{{\rm det}V_1(\cos\theta_{\rm inc})}\exp(L_1^{\rm max}[\cos\theta_{\rm inc}])}. \qquad (11)$$

As noted in §3, we assume uniform priors. Appendix B describes how we compute the prior for each model listed in Table 3, and Table 4 presents the formulae that we use to compute the prior for each model. We need not specify priors for the continuum parameters; the use of the exponentiated

Gaussian line model allows us to factor the priors for the line and continuum parameters, so that when we form the likelihood ratio, the continuum priors cancel. For the same reason, the prior for $\cos\theta_{\rm inc}$ cancels out of the final expression.

The odds favoring Model S1-U over Model S1-S, and Model S2-B over Model S2-A, is[10] $\lesssim$ 1:1, indicating a roughly 50% chance that these more complex models are the correct models to select. An odds ratio of 1:1 falls far short of the 10:1 odds criterion that would indicate sufficiently strong evidence in favor of the more complex models.

5.3. Application to the Data of GRB870303

5.3.1. GRB870303 S1

We estimate the frequentist significance of the spectral feature in GRB870303 S1 by comparing fits of the PL and PL+(S1-S) models to the data (Tables 5-6, Figure 6). The significance of the reduction in $s^2_{\rm m}$, for two additional parameters, is $\alpha_{\chi^2{\rm MLR}} = 3.6 \times 10^{-5}$. For reasons discussed above in §3 and Paper III, this value is not the "true" significance that we would derive by simulating vast numbers of datasets, but is expected to be approximately correct.

In our Bayesian analysis, we apply the PL and PL+(S1-S) models to the data and use the modified Laplace approximation eq. (11) to yield an estimate of the odds favoring the continuum-plus-line model of 114:1 (Tables 5-6; Figures 6-7). This is strong evidence in support of the line hypothesis. As discussed in §3, the use of the Laplace approximation assumes that a likelihood surface has ideal multi-dimensional Gaussian form, and our reparametrization of the line model helps ensure that the likelihood surface in this analysis has approximately that ideal form. The only way to ensure accuracy of the Laplace approximation is to perform numerical integration as a check. Unlike the case for computing credible regions, where a portion of the numerical error introduced by using sparse grids of parameter values will cancel out because one is computing a ratio (eq. 8; see Tierney & Kadane 1986), accurate numerical computation of the odds requires that we use a denser grid of parameter values. Hence, we are computationally limited to performing numerical integration only over the five-dimensional parameter space of the PL+(S1-S) model (the fifth parameter is the burst photon incidence angle). This integration yields odds $\approx$ 130:1. We conclude that the use of our reparametrization and the Laplace approximation is accurate to well within a factor of two.

In Table 7, we show the frequentist confidence and Bayesian credible intervals for the parameters of the PL+(S1-S) model. We find that for any given value $\cos\theta_{\rm inc}$ in the allowed range [0.54,0.98], the confidence and credible intervals closely match, demonstrating the efficacy of our

[10]In this paper, we follow the accepted Bayesian practice of treating the odds, the ratio of average likelihoods, as a singular quantity.

line model reparametrization. The likelihood surface as a function of $\cos\theta_{\rm inc}$ is truncated (Figure 6); while this does not affect the computation of Bayesian credible intervals, it does cause the confidence intervals for $\cos\theta_{\rm inc}$ and any parameter correlated with $\cos\theta_{\rm inc}$ (most notably the continuum normalization A and slope α) to be overestimated.

5.3.2. GRB870303 S2

We determine the frequentist significance of the spectral features in GRB870303 S2 by comparing fits using the PLE and PLE+(S2-A) models to the data (Tables 5-6; Figure 6). The significance of the reduction in $s^2_{\rm m}$, for two additional parameters, is $\alpha_{\chi^2{\rm MLR}} = 1.7 \times 10^{-4}$; the odds favoring the continuum-plus-lines model is 7:1 (Tables 5-6, Figures 6-7). The line candidates in S2 are not detected, if we apply the common criterion that the significance of the candidate line must be $\leq 10^{-4}$. The difference in odds between S1 and S2 is due to the S2 data being more informative: the errors on line parameters $E_{c,1}$ and $W_{\rm E,1}$ are smaller for S2 than for S1, reducing the average likelihood of the continuum-plus-lines model, and the odds. In Table 8 we present frequentist confidence and Bayesian credible intervals. As seen in Figure 6, the likelihood surface as a function of $\cos\theta_{\rm inc}$ is truncated, leading to differences between the computed intervals that arise for the same reason as stated above for S1.

5.3.3. Joint Fits to the Combined (S1+S2) Data

We fit to the combined (S1+S2) data because fits to this more informative dataset can strengthen the statistical evidence favoring the line hypothesis. We use the same continuum-plus-lines models that we applied to the S2 data (Table 3), except that now for each model, we test whether the data request different parameter values for S1 and S2 (i.e. we test Model S2-A with $E_{1,{\rm S1}} = E_{1,{\rm S2}}$, then $E_{1,{\rm S1}} \neq E_{1,{\rm S2}}$, etc.). Using both frequentist and Bayesian methods, we find the best-fit joint line model is the S2-B model, with the values of E_1 and $W_{\rm E,2}$ equal for S1 and S2, and $W_{\rm E,1,S1} \neq W_{\rm E,1,S2}$. (We note that the best-fit two parameter model, the S2-A model, was nested within the best-fit three parameter model, the S2-B model, which in turn was nested within the modified S2-B model shown above; hence the use of the χ^2 MLR test was valid at every step of frequentist model comparison.)

The frequentist significance of the reduction in $s^2_{\rm m}$, for four additional parameters, is $\alpha_{\chi^2{\rm MLR}} = 4.2 \times 10^{-8}$, while the odds favoring the continuum-plus-lines model is 40,300:1 (Tables 5-6; Figures 8-9). In Table 9, we present frequentist confidence intervals for the parameters of the continuum-plus-lines fit. We find that while the intervals are somewhat inaccurate because of likelihood surface truncation, we can safely conclude that the second harmonic line width is consistent with zero: there is not overwhelming statistical evidence favoring the presence of the second line. We do not compute credible regions because the number of parameters is too great. We do not use the

Laplace approximation to compute approximate credible intervals because we sample the likelihood space at only at discrete intervals in $\cos\theta_{\rm inc}$, which renders difficult the computation of covariance matrices.

We conclude that the joint (S1+S2) dataset thus presents by far the strongest evidence supporting the hypothesis that spectral lines exist in gamma-ray burst spectra.

6. Discussion

In this paper, we analyze the data of GRB870303 S1 and S2 using rigorous statistical techniques developed for gamma-ray burst line candidate analysis (Loredo & Lamb 1992; G92; G93; Freeman et al. 1993, 1994; Paper III). We conclude that the line candidates exhibited by the S1 and S2 data have significances 3.6×10^{-5} and 1.7×10^{-4}, respectively, with the Bayesian odds favoring the continuum-plus-line(s) model being 114:1 and 7:1, respectively. Fits to the combined (S1+S2) data show that the best-fit line model has significance 4.2×10^{-8}, with the odds favoring it being 40,300:1. The results of these fits to the combined data makes the line candidates they exhibit the most significant yet observed, easily satisfying the most conservative line detection criteria.

The S1 and S2 data were previously analyzed by M88 and G92, who report significances for the line candidates in S2 of $\sim 10^{-3}$ and 2.1×10^{-4}, respectively. (We have corrected the significance computed by G92, because they assumed the input number of degrees of freedom for the χ^2 MLR model comparison test to be the total number of parameters in the continuum-plus-lines model, rather than the number of additional parameters used to parametrize the lines.) Both M88 and G92 assume $\theta_{\rm inc} = 37.7^\circ$. The line candidates in S2 are not detected, if we apply the criterion that the significance of the candidate line must be $\leq 10^{-4}$ (see, e.g., Palmer 1994). G92 also discovered the line candidate in the spectrum S1, computing its significance to be 1.1×10^{-6} (also corrected). G93 use a Bayesian method to analyze the line candidates, and they report the odds in favor of the line model to be 110:1 and 2.8:1 for S1 and S2 respectively.

The differences between the analyses of M88 and G92 and our analysis are summarized in Table 10. Below, we discuss how each of these differences in turn alters the computed significance and odds of the line candidates. Unless otherwise noted, we assume $\theta_{\rm inc} = 37.7^\circ$ in all fits that we perform below, to facilitate comparison between our results and those derived previously. We note that because of this assumption, the derived significances, etc., stated below may differ somewhat from analogous values presented in Table 5.

6.1. Choice of Frequentist Statistic

We use the s^2 statistic with variances derived from the model count rates in each energy-loss bin ($s^2_{\rm m}$). Both M88 and G92 use the s^2 statistic with variances derived from the data ($s^2_{\rm d}$). As

noted in §3 and demonstrated in Paper III, the use of $s^2_{\rm d}$ can lead to an overestimation of the significance of an absorption line, relative to that derived using $s^2_{\rm m}$. (Note that the exact opposite is true for emission lines, where the use of $s^2_{\rm d}$ is to be preferred, if the Poisson likelihood cannot be used.) The magnitude of the difference between derived significances depends upon the size of the analyzed line candidate. We find that if we fit to the S1, S2, and combined (S1+S2) data using $s^2_{\rm d}$, the calculated line significances are 3.3×10^{-6}, 1.5×10^{-5}, and 1.5×10^{-9}, respectively. If we use $s^2_{\rm m}$, the respective values are 1.2×10^{-5}, 4.0×10^{-5}, and 3.1×10^{-8}.

6.2. Choice of Model Comparison Test

In Paper III, we use simulations to compute model comparison statistic PDFs for the χ^2 MLR test, the F test (used, e.g., by M88), and the χ^2 Goodness-of-Fit (GoF) test. We use these PDFs to determine that the χ^2 MLR test is the most powerful test of the three, i.e. that the use of this particular test will result in the highest rate of line detection, if lines are present in the data. Because it is the most powerful test, we use the χ^2 MLR test in this paper.

Application of the F test (with test statistic $\frac{P_2}{\Delta P}\frac{\Delta s^2_{\rm m}}{s^2_{\rm m}}$) to the S1, S2, and combined (S1+S2) data results in significance estimates of 6.7×10^{-6}, 3.3×10^{-4}, and 1.1×10^{-7}, respectively, as opposed to 1.2×10^{-5}, 4.0×10^{-5}, and 3.1×10^{-8} for the χ^2 MLR test. The F test renders the candidate line in the S1 data more significant because of the unusually small value of $s^2_{\rm m}$ for S1 (22.25 for 34 degrees of freedom). (We note that this does not make the F test more powerful in this particular case, because test power is computed from the PDF of the model comparison test statistic calculated assuming the truth of the alternative hypothesis, and not from the results of fits to a single dataset.)

The application of the χ^2 GoF test, in which the $s^2_{\rm m,c}$ is compared to the χ^2 distribution for $N - P_c$ degrees of freedom, to the S1, S2, and combined (S1+S2) data leads to significances 0.15, 0.03, and 0.02. The line candidates would not be considered detected, if we assume a significance criterion 10^{-4}. We note that if we apply the most generally-used threshold criterion of 0.05, the line candidate of S1 would still not be detected. This is a result of the unusually small value of $s^2_{\rm m}$ for the continuum fit to S1.

6.3. Use of Model Comparison to Select Continua

In §4, we describe the method with which we determine the best-fit continuum model for the S1, S2, and combined (S1+S2) data, while also determining which low-energy PC bins to include in fits. Fenimore et al. (1988), in their analysis of GRB880205, were the first to apply a number of different continuum models to data. They adopt a three-segment power law as representative of all possible models, after determining that the choice of continuum has little effect upon the detection of lines in these data. An antecedent of the method we prescribe in this paper was used

by G92 and G93, but they did not test either the PLE or Band et al. models, nor did they use model comparison to determine the usable range of PC bins. In both works, PC 10 is adopted as the lowest usable bin ($E_{\rm low} \approx 5.7$ keV).

In Table 11, we show how the results of fits to S1 and S2 change if we apply the BPL model used by G92, and the Band et al. model, to the data. We also examine how our results change if we limit ourselves to fitting to the data in PC 10-14 only, the PC bin range used by G92. We find that using the Band et al. model leads to *increases* in line significance, most notably for the fit to S1. While initially encouraging, this result does *not* actually strengthen the evidence supporting the existence of lines in these data, despite the strong Bayesian prior supporting the Band et al. model. This is because in addition to the model prior, we must take into account our prior expectation for the values of each model parameter, either qualitatively or quantitatively. In the particular case of the fit to the data of S1, the inclusion of the (unrequested) second power-law segment causes the best-fit model parameter values to deviate strongly from their expected values. For instance, the best-fit exponential cutoff energy does not lie within its characteristic range (>100 keV); instead, it is $\approx$ 10 keV. The model is attempting to fit what remains of the (no longer statistically significant) low-energy spectral rollover at energies $\approx$ 5 keV (Figure 10). This causes an increase in the continuum flux at 20 keV, increasing both the equivalent width needed to fit the data in the line region (from 9.84 to 10.7 keV) and the significance of the line. The increase in significance is greatly reduced when the lowest energy bins PC 8-9 are removed from the fit. Also, we find that we cannot compute the odds favoring the continuum-plus-line model if we use the Band et al. model. Parameter values along the Band et al. model space boundary defined by $\alpha_1 = \alpha_2$ are highly probable with respect to the mode (because the slope of the unrequested second power-law segment tends towards the slope of the first power-law segment), and because of this boundary, our fitting program was unable to estimate the covariance matrix values for the model parameters.

The fit of the Band et al. model to the S1 data demonstrates how including unjustified continuum parameters in the fit can alter the computed line significance. We feel that Briggs et al. (1998) provide another demonstration with their analysis of the emission-like line candidate of GRB941017, which was observed by the BATSE SDs. Their philosophy differs from that espoused in this paper: they contend that to demonstrate the existence of a line in this (or any) burst, one must show that the data require the line regardless of whichever reasonable continuum model is assumed. The use of a Band continuum model plus two-parameter line to fit the GRB941017 data collected by BATSE SD 0 results in a line candidate significance of 7×10^{-5}. After adding a low-energy spectral break to the continuum (which introduces two additional continuum parameters), the significance is decreased to 0.04. Thus they feel that they cannot prove the spectral feature is a line. We feel that there are two problems with this approach, one observational, and the other methodological. First, such breaks have not been observed in any other continuum spectrum, in particular those of bursts observed by the *Ginga* GBD, whose low-energy coverage is superior to that of the BATSE SDs. Hence we feel that the proposed continuum shape may not be reasonable. Second, Briggs et

al. do not use model comparison to justify that the additional continuum parameters introduced with the low-energy power law segment are necessary to adequately fit the data.

6.4. Use of Model Comparison to Select Line Models

Fitting to data with models that have more free parameters than necessary can lead to a marked reduction in derived line significance. The moderate resolution data collected by the *Ginga* GBD lack the informative power to require that each line candidate be fit with a line model parametrized by line-centroid energy, equivalent width, and full-width at half-maximum, with each value freely varying. This fact has come to be recognized through successive analyses of *Ginga* GBD data. Initially, analyses of harmonically spaced line candidates by M88, Fenimore et al., and G92[11] featured models containing two lines with six independently-varying parameters. Yoshida et al. 1991 and G92[12] reduce the number of free parameters to five, by testing models in which the line-centroid energies are harmonically related ($E_2 = 2E_1$). A further step towards model simplification is taken by G93, who test a four-parameter line model with harmonically related values of $E_{\rm n}$ and $W_{\frac{1}{2},{\rm n}}$; they also test a two-parameter line model in fits to the S1 data, assuming that the line is saturated ($W_{\frac{1}{2}} \approx W_{\rm E}$). In this work, we push model simplification to its limits, by testing both the saturated line model of G93 in fits to the S1 data and the two-free-parameter S2-A model in fits to S2.

In Table 12, we demonstrate the effect of including unnecessary line model parameters in fits to the S1 and S2 data, fitting the former with the three-parameter unsaturated line model (S1-U), and the latter with five- and six-parameter models. For S1, the addition of a parameter causes no change in $s^2_{\rm m}$ (because the mode lies at a parameter space boundary), whereas for S2, we find that each additional parameter lowers $s^2_{\rm m}$ by ≈ 1, which is just what we expect if we include in the fit parameters that the data do not request.

6.5. Effect of the Parametrization and Choice of Prior on Bayesian Odds

Our Bayesian analysis differs from that reported in G93 in that we scale the continuum amplitude and energy cutoff parameters logarithmically. This helps create a likelihood surface that more closely resembles a multi-dimensional Gaussian, and thus makes the estimation of the covariance matrix more accurate. We find that while this change has little effect upon the odds favoring the line hypothesis for S1, it does increase the odds for S2 by nearly factor of two (from 8.7:1 to 14:1, for the S2-A model with $\theta_{\rm inc} = 37.7°$, and for our chosen PC bin range).

---

[11]Specifically, for their computation of the line candidate significance for the S2 data.

[12]For their estimation of parameter values for S2.

The authors would like to thank the referee, David Band, for his careful reading of the text and his many helpful comments. This research was supported in part by NASA Graduate Student Research Fellowships NGT 50778 (PEF) and 50617 (CG), and NASA Grants NAGW 830, NAGW5-1868, and NAGW5-1464.

A. The $W_{\rm E}$-$W_{\frac{1}{2}}$ Parametrization

The equivalent width, $W_{\rm E}$, of an exponentiated Gaussian line $G(E)$ in eq. (10) is

$$\begin{aligned} W_{\rm E}(E,\beta,\sigma) &= \int_0^\infty dE \frac{C(E)-EL(E)}{C(E)} \\ &= \int_0^\infty dE(1 - \exp[G(E)]) \\ &= \sqrt{2}\sigma\Phi(E,\beta,\sigma), \end{aligned} \tag{A1}$$

where

$$\Phi(E,\beta,\sigma) = \int_{\frac{-E}{\sqrt{2}\sigma}}^{+\infty} dx \left[1-\exp(-\beta e^{-x^2})\right] \approx \int_{-\infty}^{+\infty} dx \left[1-\exp(-\beta e^{-x^2})\right]. \tag{A2}$$

The approximation $\Phi(E,\beta,\sigma) \approx \Phi(\beta)$ is satisfied in all cases where we infer a low-energy line candidate in data, breaking down only as $\beta \to \exp(\frac{E}{\sqrt{2}\sigma})$. In the following, the limit $\beta \to \infty$ has the meaning of $0 \ll \beta < \exp(\frac{E}{\sqrt{2}\sigma})$.

As $\beta \to 0$, the function $\Phi(\beta)$ has the limit

$$\begin{aligned} \lim_{\beta\to 0}\Phi(\beta) &= \int dx \beta e^{-x^2} \\ &= \beta\sqrt{\pi}. \end{aligned} \tag{A3}$$

As $\beta \to \infty$, the approximate integrand in eq. (A2) behaves approximately as a box function $B(x)$, where

$$B(x) = \begin{cases} 1, & \text{if } |x| < x_0 \ ; \\ 0, & \text{otherwise.} \end{cases} \tag{A4}$$

We estimate x_o by assuming that $\beta e^{-x_0^2} = 1$, or

$$x_0 = \sqrt{\log\beta}. \tag{A5}$$

Thus

$$\lim_{\beta\to\infty}\Phi(\beta) \approx 2\sqrt{\log\beta}. \tag{A6}$$

Differentiating $\Phi(\beta)$, we find that for all β,

$$\frac{d\Phi}{d\beta} > 0 \quad \text{and} \quad \frac{d^2\Phi}{d\beta^2} < 0. \tag{A7}$$

We may invert the mapping $\beta \rightarrow \Phi(\beta)$ for all values of β, although for even moderate values of Φ the corresponding value of β may be very large. It is numerically straightforward to invert Φ and conclude the reparametrization $(\sigma,\beta) \rightarrow (\sigma,W_{\rm E})$.

We use the physical full-width at half-maximum of the line itself (*not* of the Gaussian) to define a more physically meaningful parametrization:

$$\frac{1-\exp[G(E+W_{\frac{1}{2}}/2)]}{1-\exp[G(E)]} \;=\; \frac{1}{2}. \tag{A8}$$

We invert this equation, and use eq. (10), to write $W_{\frac{1}{2}}$ as:

$$W_{\frac{1}{2}} \;=\; 2\sqrt{2}\sigma\left\{\log(\beta)-\log\left[\log\left(\frac{2}{1+e^{-\beta}}\right)\right]\right\}^{\frac{1}{2}}. \tag{A9}$$

It follows that

$$\lim_{\beta\rightarrow 0} W_{\frac{1}{2}} \;=\; 2\sigma\sqrt{2\log 2}, \tag{A10}$$

and that

$$\lim_{\beta\rightarrow \infty} W_{\frac{1}{2}} \;=\; 2\sigma\sqrt{2(\log\beta-\log(\log 2))}. \tag{A11}$$

The reparametrization $(\sigma,\beta) \rightarrow (W_{\rm E},W_{\frac{1}{2}})$ is simplified by the observation that the ratio $r = W_{\rm E}\, W_{\frac{1}{2}}^{-1}$ depends only on β. From eqs. (A1), (A3), and (A10), we find

$$\lim_{\beta\rightarrow 0} \frac{W_{\rm E}}{W_{\frac{1}{2}}} \;=\; 0, \tag{A12}$$

while from eqs. (A1), (A6), and (A11), we find

$$\lim_{\beta\rightarrow \infty} \frac{W_{\rm E}}{W_{\frac{1}{2}}} \;=\; 1. \tag{A13}$$

The ratio $W_{\rm E}/W_{\frac{1}{2}}$ is nearly, but not quite, a monotonic function of the unnormalized Gaussian amplitude β: it rises sharply from zero, reaching $W_{\rm E}/W_{\frac{1}{2}} = 1$ when $\beta \approx 4.75$ and peaking at ≈ 1.015 when $\beta = \beta_o \approx 18.7$, before tapering off to 1 as $\beta \rightarrow \infty$ (Figure 5). Thus the line begins to saturate when $\beta \approx 4.75$ and approaches a square well shape as $\beta \rightarrow \infty$. An observed line has a value of $W_{\rm E}/W_{\frac{1}{2}}$ which falls in the range $0 \leq W_{\rm E}/W_{\frac{1}{2}} \leq 1.015$ (and therefore β in the range $0 \leq \beta \leq \beta_o$) unless it is highly saturated. We constrain β to this range, with little loss in generality, as statistical fits made without this constraint will differ very little from those made with it, unless the S/N of the line is extremely large.

B. Bayesian Prior Probability Distribution for the $W_{\rm E}$-$W_{\frac{1}{2}}$ Parametrization

There are no standard rules for determining the range and shape of the prior probability distribution in Bayesian methodology (see, e.g., Loredo 1992 and references therein). In this paper, we seek to assign priors that are "least informative." We assume a uniform, i.e. flat, distributions, bounded in a physically meaningful way.

For a single line, we use the product rules of probability theory to expand the prior:

$$p(\hat{E}, \hat{W}_{\rm E}, \hat{W}_{\frac{1}{2}}|I) \;=\; p(\hat{W}_{\frac{1}{2}}|\hat{W}_{\rm E}, \hat{E}, I)\; p(\hat{W}_{\rm E}|\hat{E}, I)\; p(\hat{E}|I). \tag{B1}$$

I represents background information about the experiment, such as detector bandpass, which allows us to specify a flat and bounded distribution of the line-centroid energy E:

$$p(\hat{E}|I) = \frac{1}{E_{\rm high} - E_{\rm low}}. \tag{B2}$$

If $\hat{E} < \frac{1}{2}E_{\rm high}$, we may specify $p(\hat{W}_{\rm E}, \hat{E}|I)$ by assuming

$$W_{\rm E} \leq \eta W_{\frac{1}{2}} \leq 2\eta(\hat{E} - E_{\rm low}), \tag{B3}$$

where $\eta \approx 1.015$, the maximum value of the ratio $W_{\rm E}/W_{\frac{1}{2}}$. A larger value of $W_{\frac{1}{2}}$ would lead us to infer that there is a low-energy rollover in the spectrum, and not a line candidate. Thus

$$p(\hat{W}_{\rm E}, \hat{E}|I) = \frac{\eta}{2(\hat{E} - E_{\rm low})}. \tag{B4}$$

The prior for a saturated line is simply the product of eqs. (B2) and (B4). If the line is not saturated, we use eq. (B3) to specify the prior for $W_{\frac{1}{2}}$:

$$p(\hat{W}_{\frac{1}{2}}|\hat{W}_{\rm E}, \hat{E}, I) = \frac{\eta}{\hat{W}_{\frac{1}{2}}}. \tag{B5}$$

The product of eqs. (B2), (B4), and (B5) gives the prior for an unsaturated line.

Assignment of the priors for two lines follows a similar procedure. We note three major differences:

- if the model has harmonically spaced lines, the prior range for E_1 is reduced: $p(\hat{E}_1|I) = (\frac{E_{\rm high}}{2} - E_{\rm low})^{-1}$;
- the prior ranges for both $W_{\rm E,1}$ and $W_{\rm E,2}$ are adapted to take into account the fact that the two lines cannot overlap and be identified as two separate lines;
- and if the model has lines that are not harmonically spaced, then $p(\hat{E}_2|\hat{E}_1)p(\hat{E}_1|I) = [(E_{\rm high} - \hat{E}_1)(E_{\rm high} - E_{\rm low})]^{-1}$.

REFERENCES

Alexander, S. G., & Mészáros, P. 1989, ApJ, 344, L1

Atteia, J.-L., et al. 1987, ApJS, 64, 305

Band, D., et al. 1992, Exp. Astr., 2, 307

Band, D., et al. 1993, ApJ, 413, 281

Band, D., et al. 1995, ApJ, 447, 289

Band, D., et al. 1996, ApJ, 458, 746

Briggs, M. S., Band, D. L., Preece, R. D., Pendleton, G. N., Paciesas, W. S., Ford, L., & Matteson, J. L. 1996, in Gamma-Ray Bursts: 3rd Huntsville Symposium, ed. C. Kouveliotou, M. F. Briggs, & G. J. Fishman (New York: AIP), 153

Briggs, M. S., Band, D. L., Preece, R. D., Pendleton, G. N., Paciesas, W. S., & Matteson, J. L. 1998, in Gamma-Ray Bursts: 4th Huntsville Symposium, ed. C. Meegan, R. Preece, & T. Koshut (New York: AIP), in press

Briggs, M. S., et al. 1999, in preparation

Djorgovski, S., Kulkarni, S. R., Bloom, J. S., Frail, D. A., Chaffee, F., & Goodrich, R. 1999, GCN Circ. 189

Djorgovski, S., Kulkarni, S. R., Bloom, J. S., Goodrich, R., Frail, D. A., Piro, I., & Palazzi, E. 1998, ApJ508, L17

Eadie, W. T., Drijard, D., James, F. E., Roos, M., & Sadoulet, B. 1971, Statistical Methods in Experimental Physics, (Amsterdam: North-Holland)

Fenimore, E. E., et al. 1988, ApJ, 335, L71

Freeman, P. E., Graziani, C., Lamb, D. Q., & Loredo, T. J. 1994, in Gamma-Ray Bursts, ed. G. J. Fishman, J. J. Brainerd, & K. Hurley (New York: AIP), 677

Freeman, P. E., Lamb, D. Q., Fenimore, E. E., & Loredo, T. J. 1993, in Compton Gamma-Ray Observatory, ed. M. Friedlander, N. Gehrels, & D. J. Macomb (New York: AIP), 922

Freeman, P. E., et al. 1999a, ApJ, this issue (Paper II)

Freeman, P. E., et al. 1999b, in preparation (Paper III)

Goodman, J. 1986, ApJ, 308, L47

Graziani, C. 1990, Investigation of the "Low χ^2" Effect in the Ginga Gamma-Ray Burst Detector Data, Internal Report, University of Chicago

Graziani, C., et al. 1992, in Gamma Ray Bursts: Observations, Analyses, and Theories, ed. C. Ho, R. Epstein, & E. Fenimore (Cambridge: Cambridge Univ. Press), 407 (G92)

Graziani, C., Lamb, D. Q., Loredo, T. J., Fenimore, E. E., Murakami, T., & Yoshida, A. 1993, in Compton Gamma-Ray Observatory, ed. M. Friedlander, N. Gehrels, & D. J. Macomb (New York: AIP), 897 (G93)

Hueter, G. J. 1987, PhD Thesis, UC San Diego

Isenberg, M., Lamb, D. Q., & Wang, J. C. L. 1998, ApJ, 493, 154

Kass, R. E., & Raftery, A. E. 1995, JASA, 90, 773

Kelson, D. D., Illingworth, G. D., Franx, M., Magee, D., & van Dokkum, P. G. 1999, IAUC 7096

Klebesadel, R. W., Strong, I. B., & Olson, R. A., ApJ, 182, L85

Kulkarni, S. R., et al. 1998, Nature, 393, 35

Lampton, M., Margon, B., & Bowyer, S. 1976, ApJ, 208, 177

Loredo, T. J. 1992, in Statistical Challenges in Modern Astronomy, ed. E. Feigelson & G. Babu (New York: Springer-Verlag), 275

Loredo, T. J., & Lamb, D. Q. 1992, in Gamma Ray Bursts: Observations, Analyses, and Theories, ed. C. Ho, R. Epstein, & E. Fenimore (Cambridge: Cambridge Univ. Press), 414

Loredo, T. J., & Wasserman, I. M. 1995, ApJS, 96, 261

Loredo, T. J., & Wasserman, I. M. 1998a, ApJ, 502, 75

Loredo, T. J., & Wasserman, I. M. 1998b, ApJ, 502, 108

Mazets, E. P., Golenetskii, S. V., Aptekar, R. L., Gurian, IU. A., & Ilinskii, V. N. 1980, Sov Ast Let, 6, 372

Mazets, E. P., Golenetskii, S. V., Aptekar, R. L., Gurian, IU. A., & Ilinskii, V. N. 1981, Nature, 290, 378

Metzger, M., et al. 1997, Nature, 387, 878

Mészáros, P., & Rees, M. J. 1997, ApJ, 476, 232

Miller, G. S., Epstein, R. I., Nolta, J. P., & Fenimore, E. E. 1991, Phys. Rev. Lett., 66, 1395

Miller, G. S., Epstein, R. I., Nolta, J., & Fenimore, E. E. 1992, in Gamma Ray Bursts: Observations, Analyses, and Theories, ed. C. Ho, R. Epstein, & E. Fenimore (Cambridge: Cambridge Univ. Press), 423

Murakami, T., et al. 1988, Nature, 335, 234 (M88)

Murakami, T., et al. 1989, PASJ, 41, 405

Palmer, D., et al. 1993, in Compton Gamma-Ray Observatory, ed. M. Friedlander, N. Gehrels, & D. J. Macomb (New York: AIP), 892

Palmer, D., et al. 1994, ApJ, 433, 77

Stanek, K. Z., Paczyński, B., & Goodman, J. 1993, ApJ, 413, 7

Tierney, L., & Kadane, J. B. 1986, JASA, 81, 82

Ulmer, A., & Goodman, J. 1995, ApJ, 442, 67

van Paradijs, J., et al. 1997, Nature, 386, 686

Wang, J. C. L., et al. 1989, Phys. Rev. Lett., 63, 1550

Wang, J. C. L., Wasserman, I., & Salpeter, E. E. 1988, ApJS, 68, 735

Yoshida, A., et al. 1989, PASJ, 41, 509

Yoshida, A., Murakami, T., Nishimura, J., Kondo, I., & Fenimore, E. 1991, PASJ, 43, L69

This preprint was prepared with the AAS LaTeX macros v5.0.

Fig. 1.— *Ginga* Proportional Counter (PC; top) and Scintillation Counter (SC; bottom) time histories of GRB870303. The PC data is presented in 1 s bins, the SC data in 0.5 second bins. The burst triggered the recording of *Ginga* burst-mode data at ≈ 16 s; the preceding 16 s of burst-mode data, in memory at the time of the trigger, were recorded and not overwritten. Burst-mode lasts for 64 seconds. Epochs S1 (4 seconds) and S2 (9 seconds) are shown; the midpoints of S1 and S2 are separated by 22.5 seconds.

Fig. 2.— *Ginga* GBD count-rate spectra for intervals S1 and S2 of GRB870303, normalized by energy-loss bin width.

Fig. 3.— (a): This flow chart illustrates how we select the best-fit continuum model. We begin by comparing the simplest model (M_1) with all alternative models that have a greater number of free parameters (M_2-$M_{\rm N}$), computing the significance of the decrease in $s^2_{\rm m}$ for each ($\alpha_{1,2}$-$\alpha_{1,{\rm N}}$). If no alternative model satisfies the criterion $\alpha_{\chi^2{\rm MLR}} \leq 0.01$, we select the simplest model; otherwise, we select the simplest alternative model that fulfills the criterion and repeat the comparison process, continuing until a continuum model is selected (i.e., until no alternative model satisfies the criterion). (b): This flow chart illustrates how we select the range of usable PC bins. We do not use all PC data because of the difficulty of modeling the spectral rollover at energy-losses $\lesssim 5$ keV. The box "Select Continuum Model" refers to the flow chart in (a).

Fig. 4.— Probability contours resulting from the use of various combinations of unnormalized Gaussian amplitude and width (β,σ), equivalent width $W_{\rm E}$, and full-width $W_{\frac{1}{2}}$, to parametrize line shape. We show 1, 2, and 3σ contours, representing 68.3%, 95.5%, and 99.7% of the integrated probability. Only the $(W_{\frac{1}{2}}, W_{\rm E})$ parametrization contours, shown at lower left, show the elliptical behavior required to use eq. (6) to compute the Bayesian odds.

Fig. 5.— The ratio of line equivalent width, $W_{\rm E}$, to line full-width, $W_{\frac{1}{2}}$, as a function of Gaussian amplitude β. This ratio is not a function of the Gaussian width σ. It reaches 1 (short dashed line) when $\beta \approx 4.75$ and peaks at $r \approx 1.015$ when $\beta = \beta_o \approx 18.75$ (long dashed line). We set $\beta = \beta_o$ when fitting saturated lines to data.

Fig. 6.— Values of the fitting statistics $s^2_{\rm m}$ (squares) and L (circles) as a function of $\cos\theta_{\rm inc}$, for fits to the data of GRB870303 S1 (top) and GRB870303 S2 (bottom). Unfilled shapes represent continuum model fits, while filled shapes represent continuum-plus-line(s) model fits. Any jaggedness in fitting statistic values as a function of angle reflects the use of Monte Carlo simulations to create *Ginga* GBD response matrices. Jaggedness is more apparent in fits to the data of S2 because they are more informative (i.e. the number of counts per bin is higher for S2 than S1).

Fig. 7.— Best-fit continuum-plus-line(s) photon number spectra (top), observed count-rate spectra and best-fit continuum-plus-line(s) count-rate spectra (middle), and residuals of the best-fit in units of σ (bottom) for the intervals S1 (left) and S2 (right) of GRB870303.

Fig. 8.— Same as Figure 6, for the joint fits to intervals S1 and S2 of GRB870303.

Fig. 9.— Best-fit continuum-plus-line(s) photon number spectra (top), observed count-rate spectra and best-fit continuum-plus-line(s) count-rate spectra (middle), and residuals of the best-fit in units of σ (bottom) for the joint fit to intervals S1 (left) and S2 (right) of GRB870303.

Fig. 10.— Best-fit photon spectra for GRB870303 S1, assuming burst photon incidence angle $\theta_{\rm inc}$ = 37.7°. The solid line shows the best-fit PL continuum model, while the dashed line shows the best-fit Band et al. continuum model.

Table 1. Continuum Models

Model	Formula
Power Law (PL)	$\frac{dN}{dE} = AE^{-\alpha}$
PL × Exponential (PLE)	$\frac{dN}{dE} = AE^{-\alpha}\exp(-\frac{E}{E_c})$
Band et al. (1993)	$\frac{dN}{dE} = \begin{cases} AE^{-\alpha_1}\exp(-\frac{E}{E_c}), & E \leq (\alpha_2-\alpha_1)E_c \\ A\left[(\alpha_2-\alpha_1)E_c\right]^{\alpha_2-\alpha_1} \times & \\ \quad \exp(\alpha_1-\alpha_2)E^{-\alpha_2}, & \text{otherwise} \end{cases}$
Broken Power Law (BPL)	$\frac{dN}{dE} = \begin{cases} AE^{-\alpha_1}, & E \leq E_b \\ AE_b^{\alpha_2-\alpha_1}E^{-\alpha_2}, & \text{otherwise} \end{cases}$
Low-Energy Rollover (NH)	$\left(\frac{dN}{dE}\right)_{\rm col} = \left(\frac{dN}{dE}\right)\exp(-A\times E^{-3})$

Note. — In the fitting code itself, it is the logarithms of the normalization A and PLE cutoff energy E_c that are varied. Also, a "pivot" energy of 20 keV is used to reduce the size of the frequentist confidence and Bayesian credible intervals for the highly correlated parameters A and α. These changes alter the likelihood surface in parameter space in such a way as to make it more closely resemble a multi-dimensional Gaussian function.

Table 2. Energy-Loss Bins and Continua Used in Analyses

Spectrum	PC Bins	SC Bins	Selected Continuum
S1	8-15	2-31	PL
S2	7-15	2-31	PLE
S1+S2	10-15	2-31	PL(S1)+PLE(S2)[a]

[a]The continuum model is a six-parameter model in which $\log A_{\rm S1}$ and $\alpha_{\rm S1}$ vary independently of $\log A_{\rm S2}$ and $\alpha_{\rm S2}$, but for which $\cos(\theta_{\rm inc})_{\rm S1} = \cos(\theta_{\rm inc})_{\rm S2}$.

Table 3. Exponentiated Gaussian Line Models

Model	Free Line Parameters
S1-S	$(E, W_{\rm E})$
S1-U	$(E, W_{\rm E}, W_{\frac{1}{2}})$
S2-A	$(E_1, W_{\rm E,1})$
S2-B	$(E_1, W_{\rm E,1}, W_{\rm E,2})$
S2-C	$(E_1, W_{\rm E,1}, W_{\frac{1}{2},1})$
S2-D	$(E_1, W_{\rm E,1}, W_{\frac{1}{2},1}, W_{\rm E,2}, W_{\frac{1}{2},2})$

Note. — Parameters not shown have values set by the values of the parameters shown; e.g., for S2-A, $E_2 = 2E_1$, $W_{\frac{1}{2},1} = \eta^{-1} W_{\rm E,1}$, $W_{\rm E,2} = 2W_{\rm E,1}$, and $W_{\frac{1}{2},2} = \eta^{-1} W_{\rm E,2}$. Not shown are variations on the S2 class of models for which $E_2 \neq 2E_1$. While these models were tested for completeness, none significantly improved fits.

Table 4. Prior Probabilities for Exponentiated Gaussian Model

Model	Prior Probability
S1-S	$p = [2\eta(\hat{E} - E_{\rm low})(E_{\rm high} - E_{\rm low})]^{-1}$
S1-U	$p = [2\hat{W}_{\rm E}(\hat{E} - E_{\rm low})(E_{\rm high} - E_{\rm low})]^{-1}$
S2-A	$p = [\frac{\eta}{3}\hat{E}_1(E_{\rm high} - 2E_{\rm low})]^{-1}$
S2-B	$p = [(2\eta\hat{E}_1 - \hat{W}_{\rm E,1})(\hat{E}_1 - E_{\rm low})(E_{\rm high} - 2E_{\rm low})]^{-1}$
S2-C	$p = [\frac{\eta}{3}\hat{W}_{\frac{1}{2},1}\hat{E}_1(E_{\rm high} - 2E_{\rm low})]^{-1}$
S2-D	$p = [\eta^2\hat{W}_{\frac{1}{2},1}\hat{W}_{\frac{1}{2},2}(2\hat{E}_1 - \hat{W}_{\frac{1}{2},1})(\hat{E}_1 - E_{\rm low})(E_{\rm high} - 2E_{\rm low})]^{-1}$

Note. — $\eta = \left(\frac{W_E}{W_{\frac{1}{2}}}\right)_{max} \approx 1.015$. $E_{\rm low}$ and $E_{\rm high}$ represent the low and high energy-loss bandpass boundaries, respectively, for the *Ginga* GBD. Not shown are the priors for variations on the S2 class of models for which $E_2 \neq 2E_1$; while these models were tested, none significantly improved fits. See Appendix B for details.

Table 5. Line Significances and Odds

Dataset	Model	$s^2_{\rm C}$ (dof)	$s^2_{\rm C+L}$ (dof)	$\alpha_{\chi^2{\rm MLR}}$	$L_{\rm C}$	$L_{\rm C+L}$	Odds
S1	S1-S	42.71 (35)	22.22 (33)	3.6×10^{-5}	49.44	60.55	114:1
S2	S2-A	49.94 (35)	32.60 (33)	1.7×10^{-4}	89.90	98.73	7:1
S1+S2	S2-B[a]	86.18 (66)	46.13 (62)	4.2×10^{-8}	126.44	147.28	40,300:1

[a]All line parameters have the same value for S1 and S2 except $W_{\rm E,1,S1} \neq W_{\rm E,1,S2}$.

Table 6. Best-Fit Parameters

	Frequentist			Bayesian		
Parameter	S1	S2	S1+S2	S1	S2	S1+S2
$\log A_{\rm S1}$[a]	-0.77	-	-0.80	-0.84	-	-0.80
$\log A_{\rm S2}$[a]	-	-0.56	-0.39	-	-0.55	-0.39
$\alpha_{\rm S1}$	1.72	-	1.75	1.67	-	1.76
$\alpha_{\rm S2}$	-	1.19	1.48	-	1.19	1.47
E_c (keV)	-	2.14	2.39	-	2.13	2.38
E_1 (keV)	21.4	21.8	21.5	21.3	21.8	21.5
$W_{E,1,\rm S1}$ (keV)	10.7	-	11.2	10.4	-	11.1
$W_{E,1,\rm S2}$ (keV)	-	2.16	2.82	-	2.21	2.73
$W_{E,2}$ (keV)	-	-	2.72	-	-	2.86
$\cos(\theta_{\rm inc})$	0.54	0.82	0.60	0.58	0.82	0.60

[a]Amplitudes at the "pivot" energy of 20 keV.

Table 7. S1: Parameter Estimation

	Par	Freq	Bayes	Par	Freq	Bayes
Best Fit	$\log A$[a]	-0.77	-0.84	E	21.4	21.3
1σ		[-1.05,-0.74]	[-1.14,-0.84]	(keV)	[20.3,22.5]	[20.0,22.5]
2σ		[-1.23,-0.70]	[-1.23,-0.73]		[19.2,23.9]	[18.7,24.0]
3σ		[-1.29,-0.67]	[-1.31,-0.66]		[18.1,25.7]	[17.5,25.8]
Best Fit	α	1.72	1.67	W_E	10.7	10.4
1σ		[1.52,1.78]	[1.47,1.70]	(keV)	[8.41,13.1]	[7.85,12.9]
2σ		[1.35,1.85]	[1.37,1.80]		[6.16,15.9]	[5.74,15.8]
3σ		[1.26,1.92]	[1.27,1.90]		[3.80,19.8]	[4.55,17.8]
Best Fit				$\cos(\theta_{\rm inc})$	0.54	0.58
1σ					[0.54,0.78]	[0.54,0.72]
2σ					[0.54,0.98]	[0.54,0.95]
3σ					[0.54,0.98]	[0.54,0.978]

[a]Amplitude at the "pivot" energy of 20 keV.

Table 8. S2: Parameter Estimation

	Par	Freq	Bayes	Par	Freq	Bayes
Best Fit	$\log A$[a]	-0.56	-0.55	E_1	21.8	21.8
1σ		[-0.60,-0.43]	[-0.63,-0.47]	(keV)	[20.3,22.5]	[21.1,22.6]
2σ		[-0.69,-0.34]	[-0.70,-0.38]		[19.2,23.9]	[20.2,23.3]
3σ		[-0.72,-0.28]	[-0.73,-0.34]		[18.1,25.7]	[19.5,24.0]
Best Fit	α	1.19	1.19	$W_{E,1}$	2.16	2.21
1σ		[1.10,1.32]	[1.15,1.31]	(keV)	[1.73,2.62]	[1.67,2.70]
2σ		[0.97,1.44]	[1.00,1.42]		[1.20,3.15]	[1.16,3.09]
3σ		[0.89,1.54]	[0.90,1.54]		[0.63,3.66]	[1.02,3.38]
Best Fit	$\log E_c$	2.14	2.13	$\cos(\theta_{\rm inc})$	0.82	0.82
1σ	(keV)	[2.04,2.25]	[2.04,2.25]		[0.70,0.94]	[0.66,0.96]
2σ		[1.96,2.41]	[1.94,2.39]		[0.58,0.98]	[0.60,0.98]
3σ		[1.88,2.58]	[1.84,2.57]		[0.54,0.98]	[0.56,0.98]

[a]Amplitude at the "pivot" energy of 20 keV.

Table 9. S1+S2: Parameter Estimation

	Par	Freq	Par	Freq
Best Fit	$\log A_{\rm S1}$[a]	-0.80	E_1	21.5
1σ		[-0.98,-0.73]	(keV)	[20.8,22.1]
2σ		[-1.11,-0.67]		[20.1,22.6]
3σ		[-1.22,-0.61]		[19.3,23.2]
Best Fit	$\alpha_{\rm S1}$	1.75	$W_{E,1,\rm S1}$	11.2
1σ		[1.61,1.83]	(keV)	[9.15,13.4]
2σ		[1.49,1.92]		[7.08,16.0]
3σ		[1.37,2.03]		[5.02,19.2]
Best Fit	$\log A_{\rm S2}$[a]	-0.39	$W_{E,1,\rm S2}$	2.82
1σ		[-0.43,-0.33]	(keV)	[2.04,3.40]
2σ		[-0.44,-0.24]		[1.35,4.00]
3σ		[-0.47,-0.22]		[0.64,4.71]
Best Fit	$\alpha_{\rm S2}$	1.48	$W_{E,2}$	2.72
1σ		[1.30,1.56]	(keV)	[1.38,4.06]
2σ		[1.12,1.67]		[0.00,5.28]
3σ		[0.98,1.74]		[0.00,6.44]
Best Fit	$\log E_c$	2.40	$\cos(\theta_{\rm inc})$	0.60
1σ	(keV)	[2.22,2.59]		[0.58,0.78]
2σ		[2.08,2.91]		[0.54,0.96]
3σ		[1.97,∞]		[0.54,0.98]

[a]Amplitude at the "pivot" energy of 20 keV.

Table 10. Analyses of GRB870303 Line Candidates

Work	Spec	$\theta_{\rm inc}$	Stat	Model Comp Test	C Model Comp?	C+L Model Comp?	Number of Line Par	Sig or Odds
M88	S2	37.7°	$s^2_{\rm d}$	F	N[a]	N	6	$\sim 10^{-3}$
G92	S1	37.7°	$s^2_{\rm d}$	χ^2 MLR	Y	N	3	1×10^{-5}
	S2				Y	N	6	2×10^{-4}
G93	S1	37.7°	L	Odds	N[b]	N	2[c]	110:1
	S2				N[d]	N	4[e]	2.8:1
This	S1	Free	$s^2_{\rm m}$	χ^2 MLR	Y	Y	2	2.2×10^{-5}
Work			L	Odds	N	Y	2	114:1
	S2		$s^2_{\rm m}$	χ^2 MLR	Y	Y	2	1.7×10^{-4}
			L	Odds	N	Y	2	7:1
	S1+S2		$s^2_{\rm m}$	χ^2 MLR	Y	Y	4	4.2×10^{-8}
			L	Odds	N	Y	4	40,300:1

[a]M88 assume a thermal cyclotron continuum.

[b]G93 apply the power-law continuum model used in G92.

[c]G93 assume the line to be saturated.

[d]G93 apply the two-segment broken power-law continuum model used in G92.

[e]G93 assume the energies and full-widths of the two lines to be harmonically related.

Table 11. Effect of Changing Continuum Model and PC Bin Range on Fits

Dataset	Continuum	PC Bins	$\alpha_{\chi^2\mathrm{MLR}}$	Odds
S1	PL	8-15	1.2×10^{-5}	119:1
	PL	10-14	5.3×10^{-6}	339:1
	Band	8-15	1.6×10^{-6}	-[a]
	Band	10-14	3.9×10^{-6}	-[a]
S2	PLE	7-15	4.0×10^{-5}	14:1
	PLE	10-14	1.1×10^{-5}	15:1
	Band	7-15	1.1×10^{-5}	81:1
	Band	10-14	4.0×10^{-6}	87:1
	BPL	7-15	2.0×10^{-5}	28:1
	BPL	10-14	5.3×10^{-5}	10:1

Note. — We use the best-fit line model for each dataset, and assume $\theta_{\mathrm{inc}} = 37.7°$.

[a] $\sqrt{\det V}$ cannot be computed because the mode is too close to a parameter space boundary.

Table 12. Effect of Increasing the Number of Line Parameters in Fits to S1 and S2

	2 Par (S1-S)	3 Par (S1-U)	2 Par (S2-A)	5 Par (S2-D)	6 Par
$s^2_{\rm m,C}$	44.84	44.84	53.91	53.91	53.91
$s^2_{\rm m,C+L}$	22.23	22.23	33.63	31.13	30.49
$\alpha_{\chi^2{\rm MLR}}$	1.2×10^{-5}	4.8×10^{-5}	4.0×10^{-5}	3.7×10^{-4}	6.7×10^{-4}
E_1 (keV)	21.2	21.2	21.8	21.8	21.3
$W_{\rm E,1}$ (keV)	9.98	9.98	2.24	3.35	3.12
$W_{\frac{1}{2},1}$ (keV)	[10.1]	10.1	[2.27]	6.20	5.55
E_2 (keV)			[43.6]	[43.6]	44.4
$W_{\rm E,2}$ (keV)			[5.48]	4.23	4.25
$W_{\frac{1}{2},2}$ (keV)			[5.54]	4.67	4.80

Note. — Values in brackets are fixed by values of other parameters (see Table 3). We assume $\theta_{\rm inc} = 37.7^\circ$.

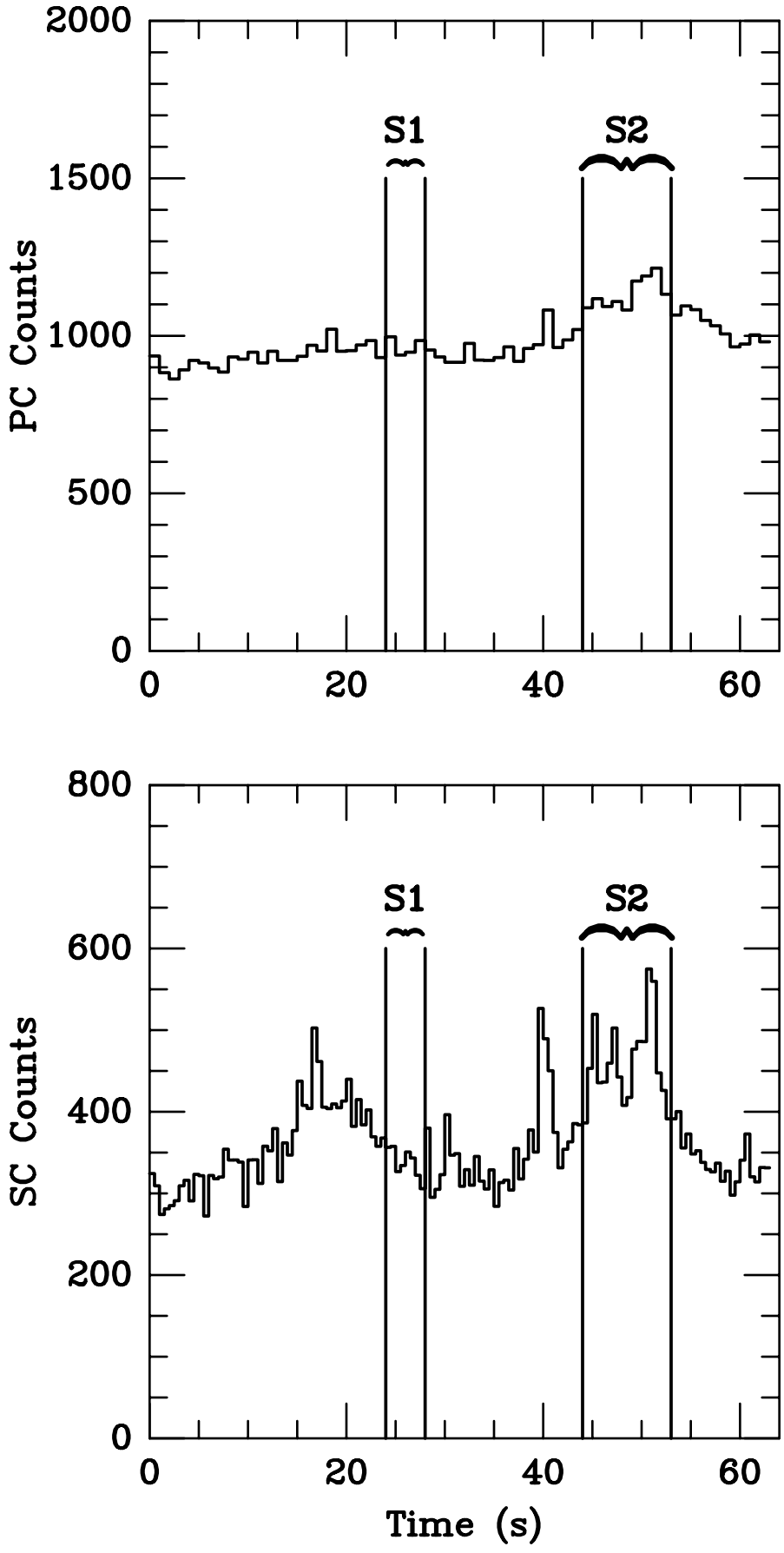
2000
1500
1000
500
0
PC Counts
S1
S2
0
20
40
60
800
600
400
200
0
SC Counts
S1
S2
0
20
40
60
Time (s)

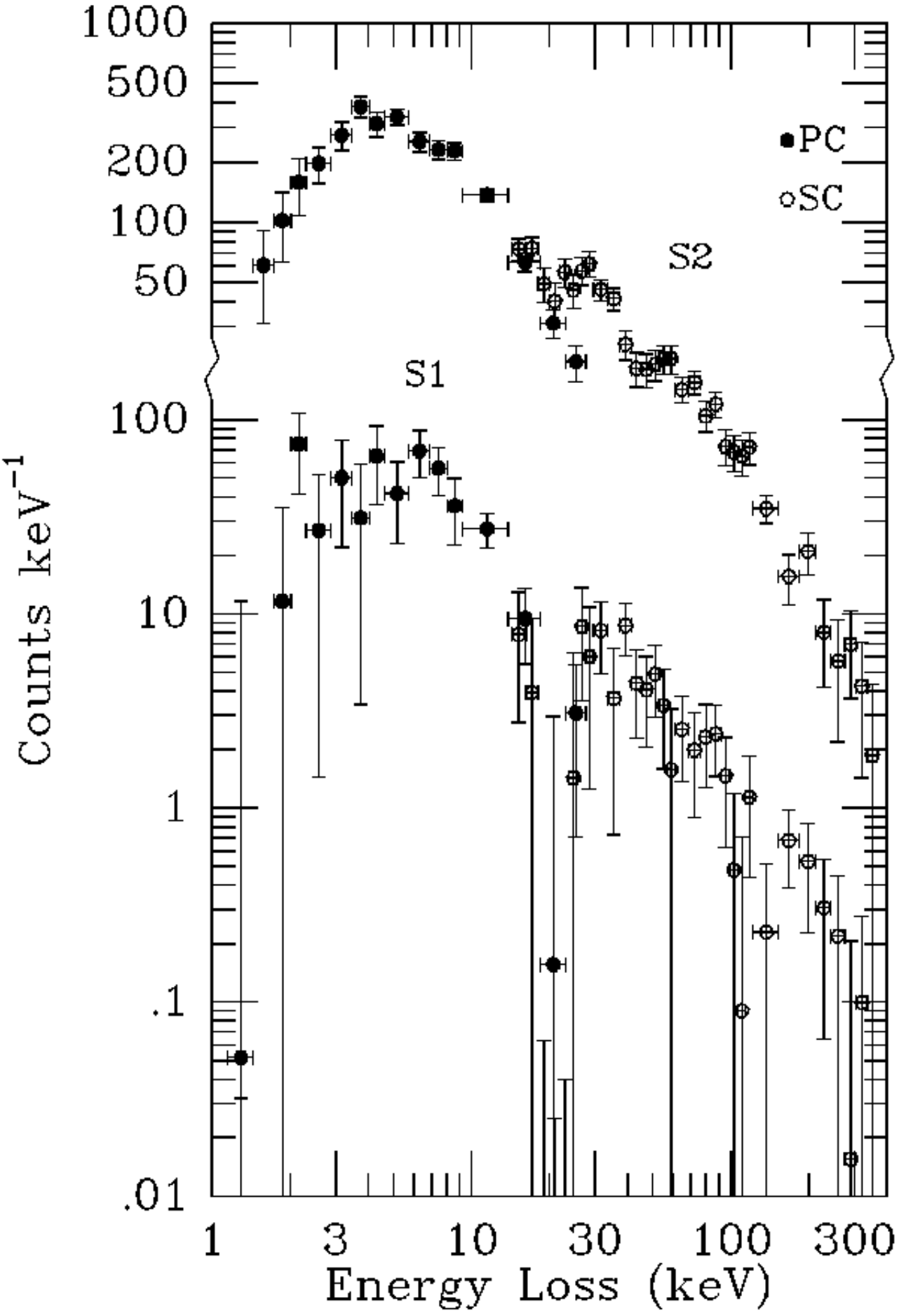
1000
500
200
100
50
100
10
1
.1
.01
PC
SC
S2
S1
Counts keV^{-1}
1
3
10
30
100
300
Energy Loss (keV)

Ginga PC Channel Selection

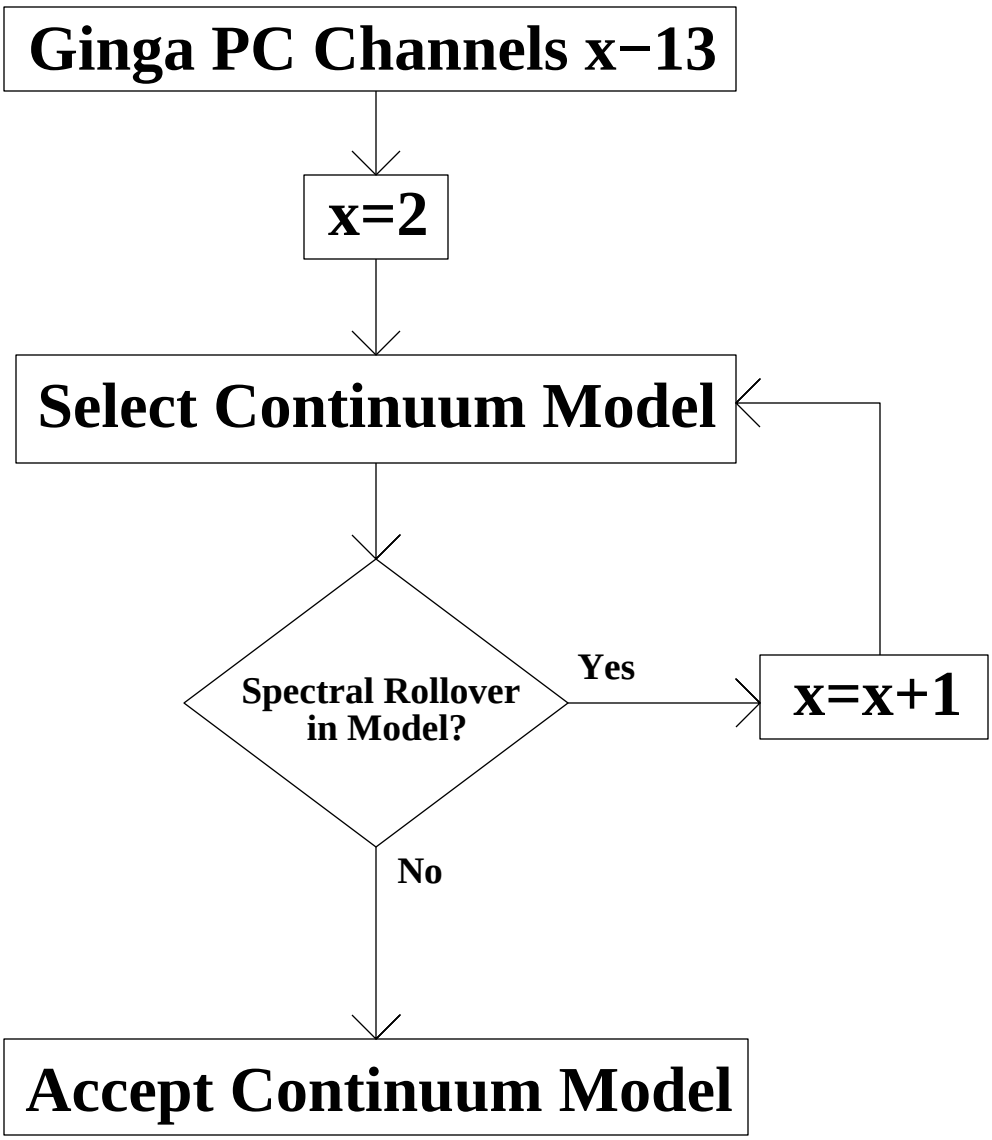

Model Selection

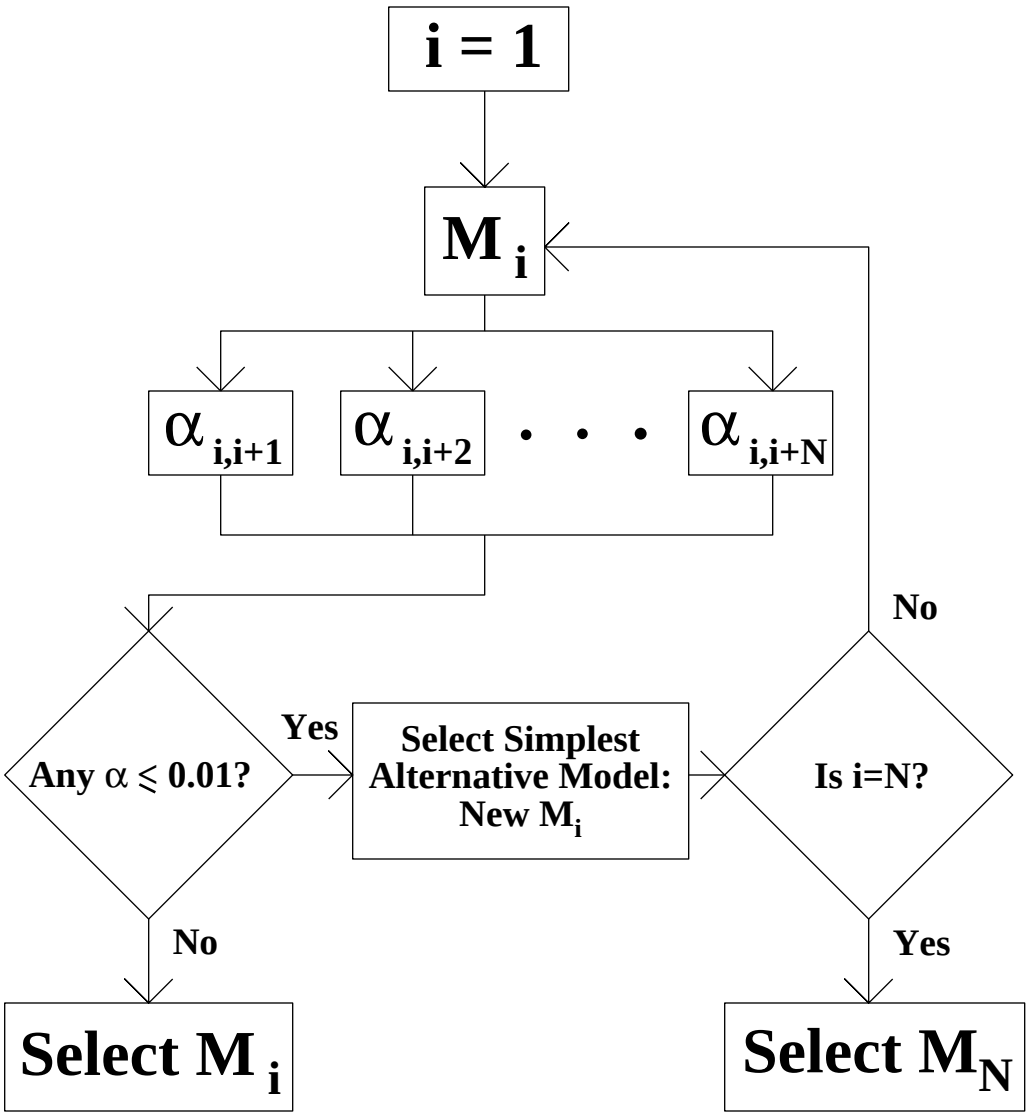

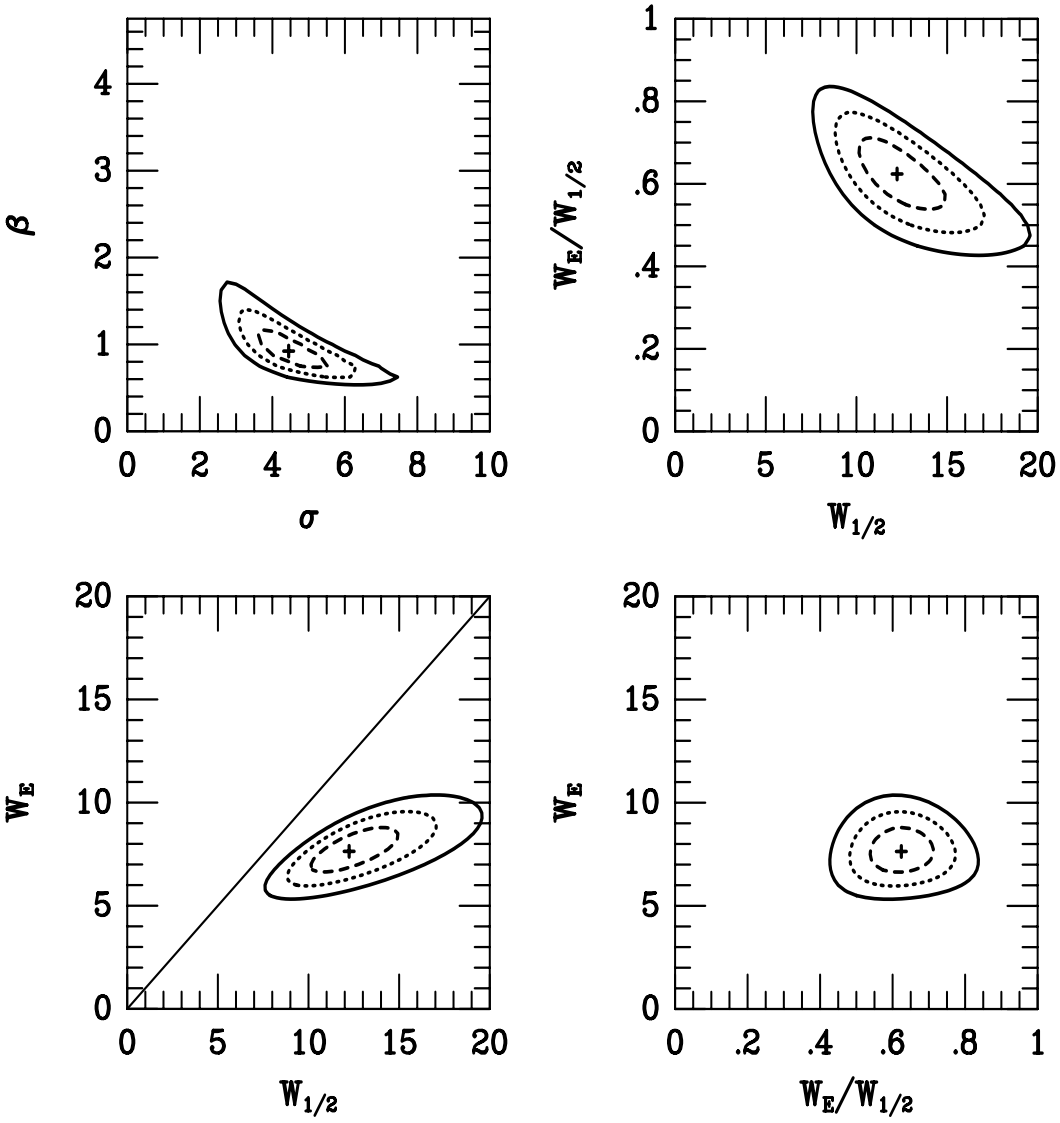
β
σ
W_E/W_1/2
W_1/2
W_E
W_1/2
W_E
W_E/W_1/2

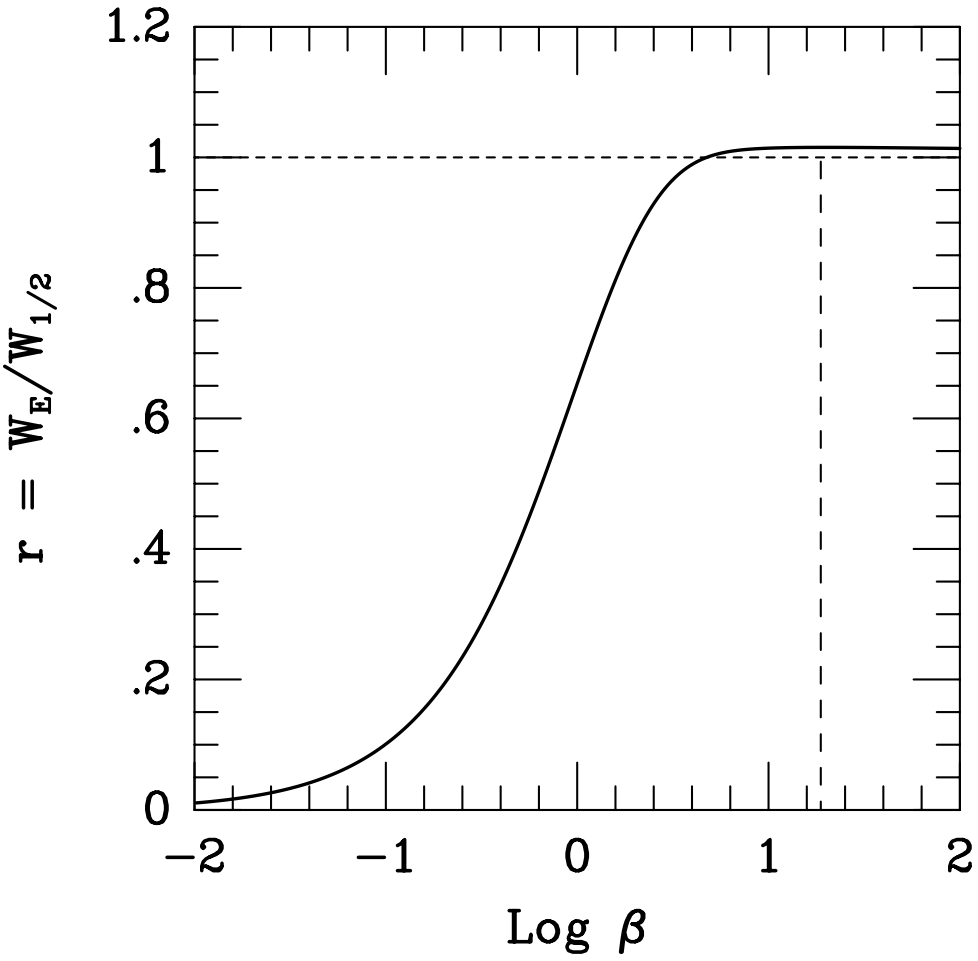
1.2
1
.8
.6
.4
.2
0
−2
−1
0
1
2
r = W_E/W_1/2
Log β

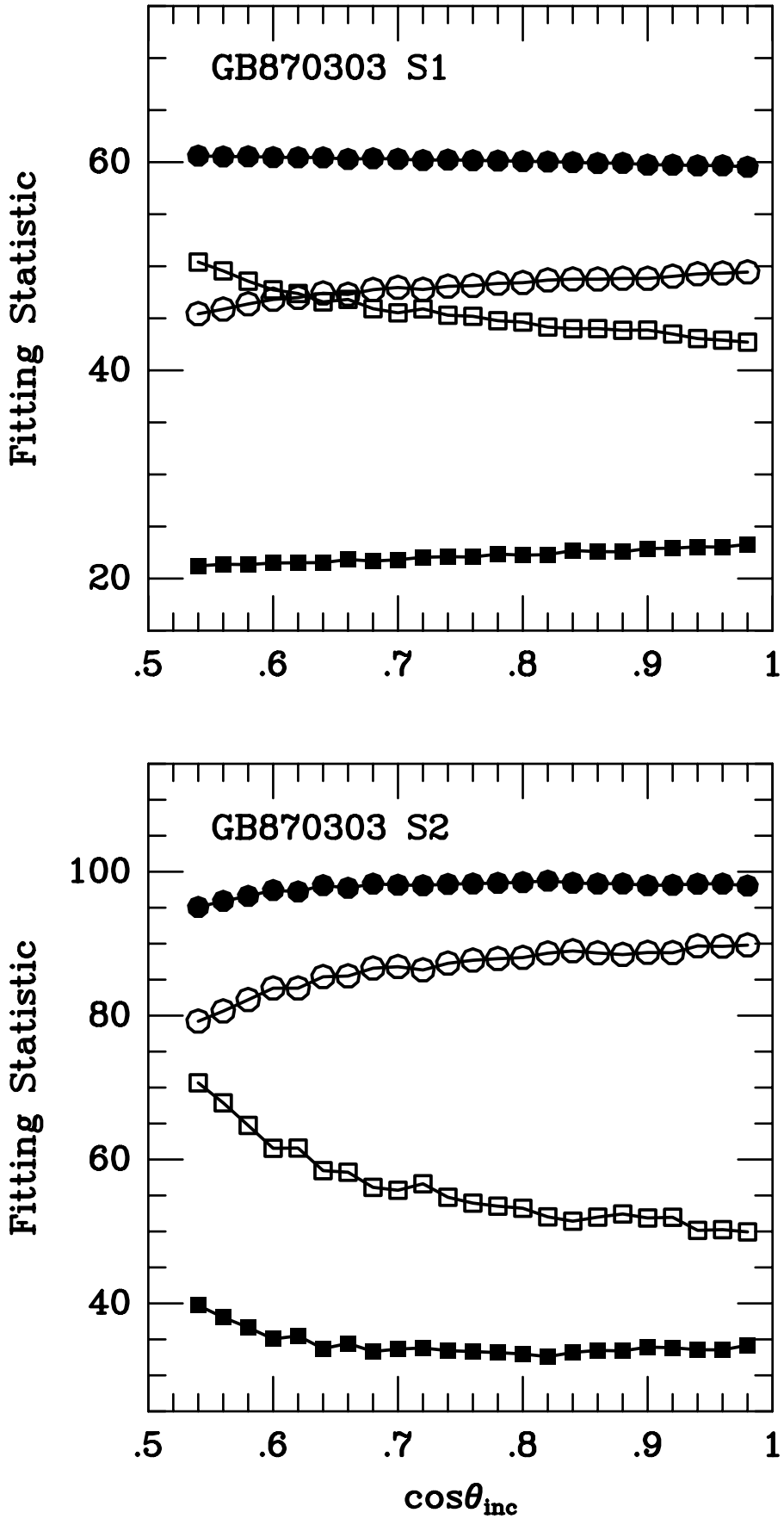
GB870303 S1
Fitting Statistic
60
40
20
.5
.6
.7
.8
.9
1
GB870303 S2
Fitting Statistic
100
80
60
40
.5
.6
.7
.8
.9
1
cosθinc

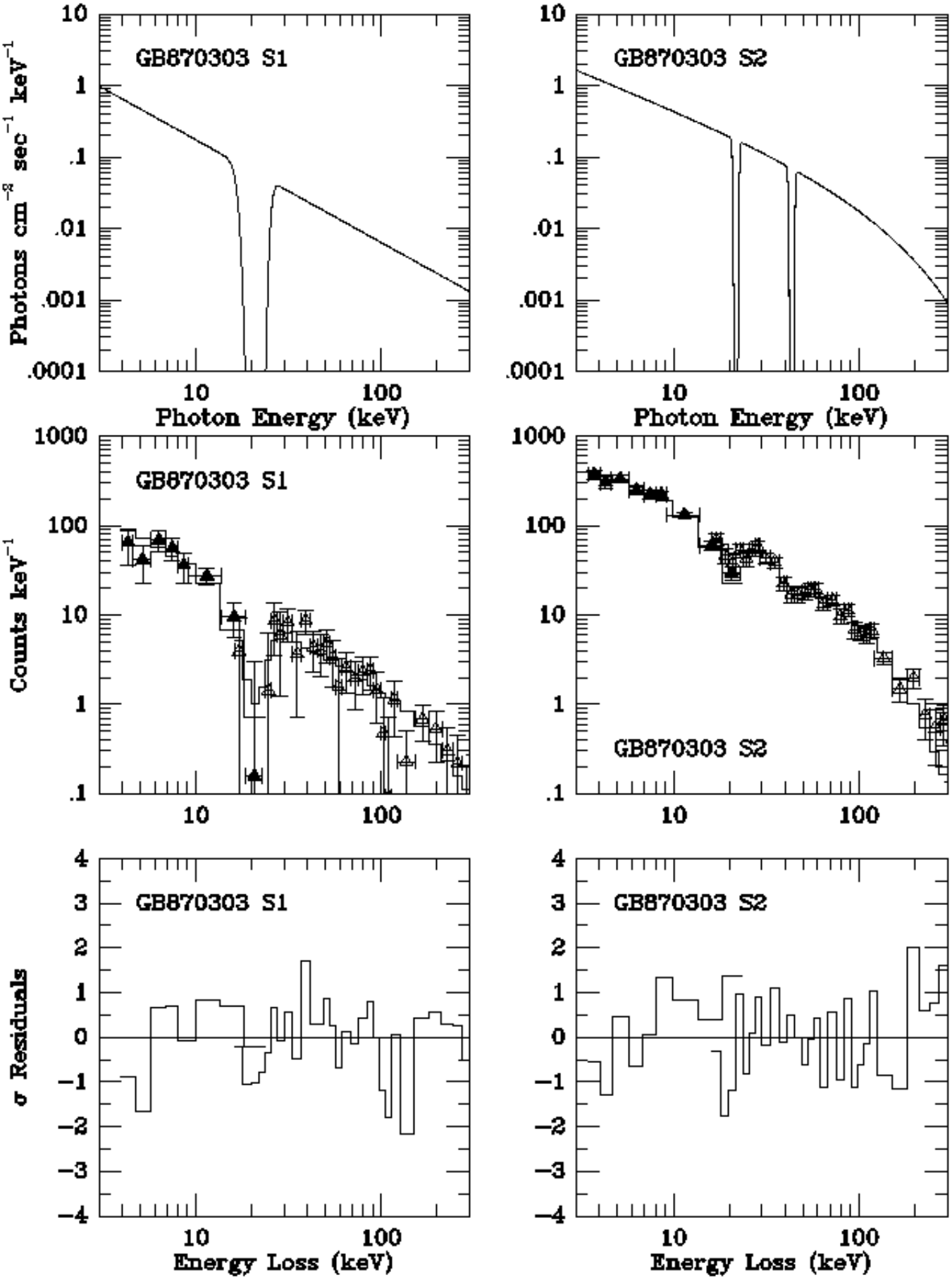
GB870303 S1
GB870303 S2
Photons cm^{-2} sec^{-1} keV^{-1}
Photon Energy (keV)
Counts keV^{-1}
σ Residuals
Energy Loss (keV)

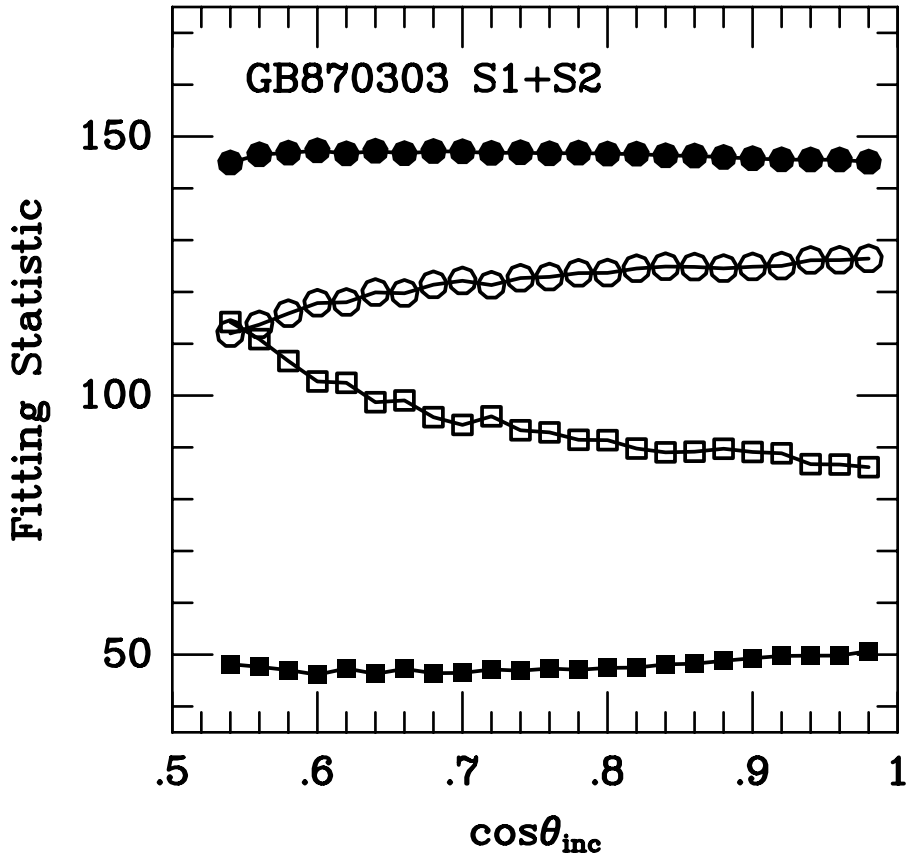
GB870303 S1+S2
150
100
50
Fitting Statistic
.5
.6
.7
.8
.9
1
cosθinc

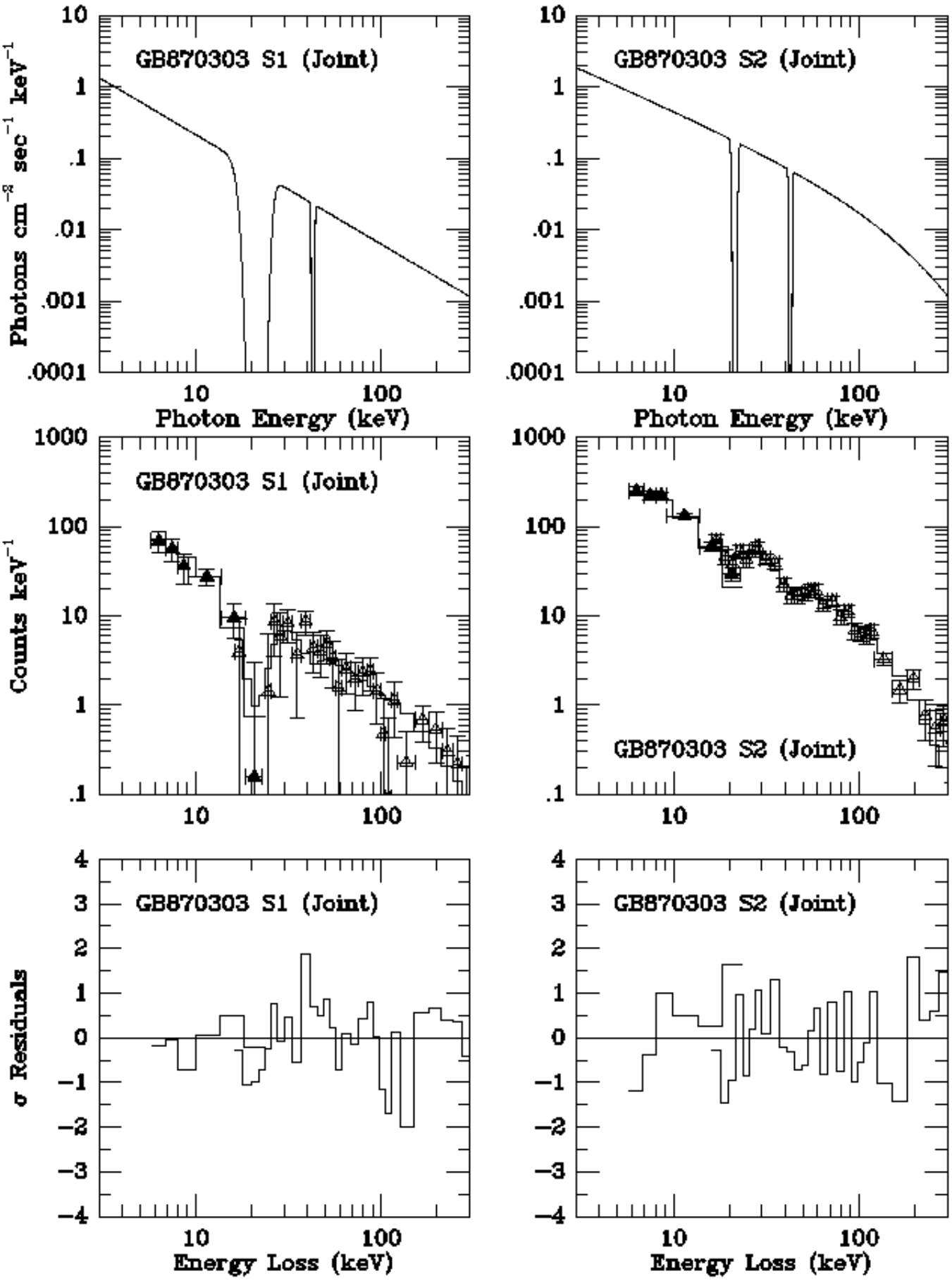
GB870303 S1 (Joint)
GB870303 S2 (Joint)
Photons cm^{-2} sec^{-1} keV^{-1}
Photon Energy (keV)
Counts keV^{-1}
σ Residuals
Energy Loss (keV)

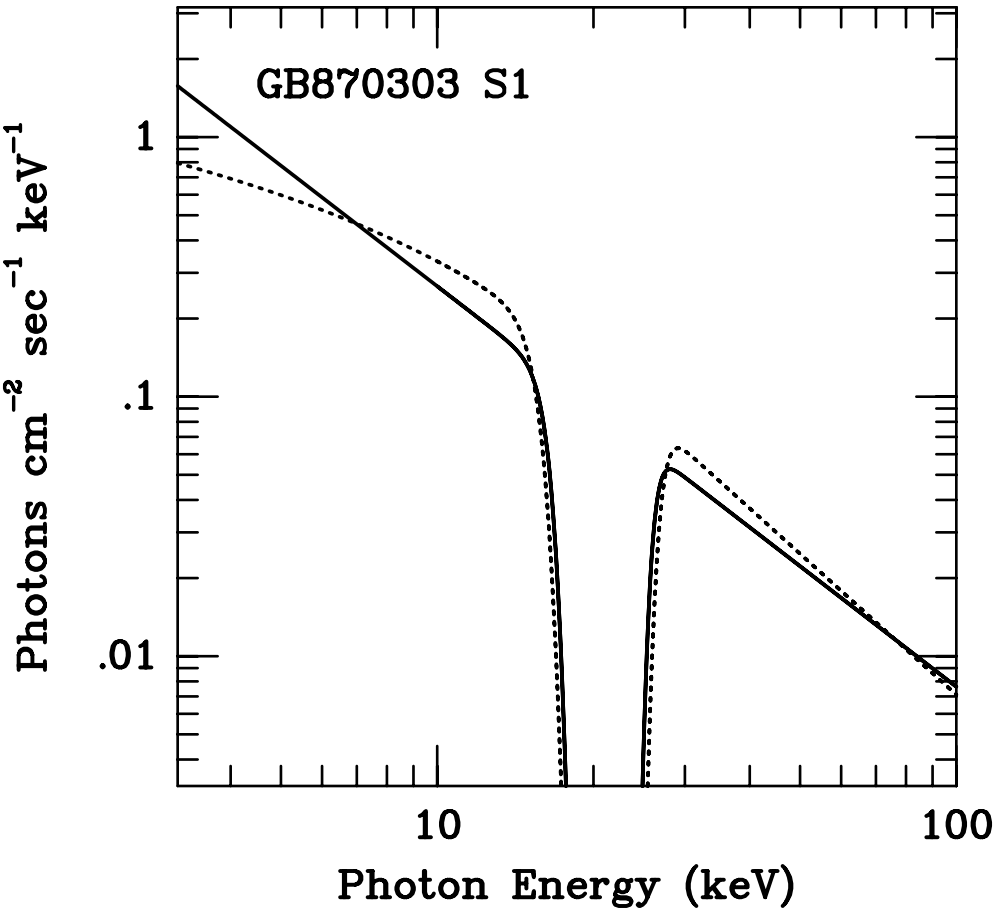
GB870303 S1
Photons cm^{-2} sec^{-1} keV^{-1}
1
.1
.01
10
100
Photon Energy (keV)